Nucleation in Confinement: A Pathway to Size-Controlled Ultra-Small Icosahedral Silver Nanoparticles

Rohan Parmar, Raj Kumar Ramamoorthy, Pierre Roblin, Nicolas Ratel-Ramond, Lise-Marie Lacroix, Isaac Rodriguez-Ruiz, Sébastien Teychené, Guillaume Viau

Nucleation in Confinement: A Pathway to Size-Controlled Ultra-Small Icosahedral Silver Nanoparticles

Rohan Parmar,[1,2] Raj Kumar Ramamoorthy,[2] Pierre Roblin,[1] Nicolas Ratel-Ramond,[2] Lise-Marie Lacroix,[2] Isaac Rodriguez-Ruiz,[1] Sébastien Teychené,[1*] Guillaume Viau[2*]

[1] *Université de Toulouse, Laboratoire de Génie Chimique, CNRS, INP, 4 allée Emile Monso F-31432 Toulouse cedex 4 France*

[2] *Université de Toulouse, Laboratoire de Physique et Chimie des Nano-Objets, INSA Toulouse, CNRS, 135 avenue de Rangueil F-31077 Toulouse cedex 4, France*

Abstract

The size and structural control of ultra-small metal nanoparticles (NPs) remains a key area of research, as their unique nanoscale properties can significantly impact their utility and applications in industry. Among the different synthesis strategies, the formation of large clusters of metal precursors in solution, which favours a confined nucleation, has been less explored. Here, we report a simple synthesis protocol of ultra-small silver nanoparticles with an icosahedral structure, a mean diameter of 3 nm and low polydispersity (down to 6%), through the reduction of $AgNO_3$ by trialkylsilanes in a solution of oleylamine (OY) and hexane. Small- and wide-angle X-ray scattering (SAXS, WAXS) and pair distribution function (PDF) analysis reveal that the Ag NP size and structure remain constant regardless of Ag and reducing agent concentrations, or temperatures up to 120°C. The lack of correlation between the final NP size and the initial Ag concentration, temperature, and reaction rate – despite variations spanning two orders of magnitude – does not align with a classical nucleation/growth mechanism of isolated monomers in solution. SAXS analysis of the precursor solutions revealed the presence of $\{OY\text{-}Ag^{(I)}\text{-}NO_3\}_n$ clusters, which interact repulsively in solution. The final Ag particle size is closely tied to the size of the Ag(I) clusters. This suggests that size control is governed by a nucleation process involving Ag atoms within the clusters. The separation of nucleation and growth appears to be achievable through nucleation confined within the repulsively interacting $\{OY\text{-}Ag^{(I)}\text{-}NO_3\}_n$ clusters. Only two factors have been found to decrease the mean NP size: increasing the OY concentration, or substituting $AgNO_3$ with silver trifluoro-sulfonate or trifluoro-acetate, which reduces the mean size, in agreement with smaller initial $Ag^{(I)}$ clusters. The advantage of this synthesis route is the very high concentration of metals that can be achieved without degrading the morphological and structural quality of the final particles.

1. Introduction

Recent years have seen a significant leap in the design and synthesis of noble metal nanoparticles with narrow size distributions and controlled morphologies[1], enabling advances in numerous applications such as catalysis,[2,3] drug delivery,[4,5] photonics,[6,7] and electronics.[8–10] Silver nanoparticles (Ag NPs) have been a key subject of study, due to their antibacterial properties, which make them promising for a wide range of biomedical applications.[11,12] Additional interest has also grown because of their unique optical properties resulting from localized surface plasmon resonance (LSPR) with applications in fields such as Surface-enhanced Raman spectroscopy (SERS),[13] biosensing,[14] or solar cells optimization.[15] High particle monodispersity can additionally promote self-assemblies into larger-scale two- and three- dimensional superlattices, whereby anisotropic interactions between neighbouring particles within this higher order may give further rise to useful collective properties. These include enhanced vibrational coherence and particular optical properties due to the near-field coupling of surface plasmons of neighbouring NPs, leading to particularly interesting applications in optics/photonics (Raman scattering) and biosensing.[16,17] Ultra-small Ag NPs, ranging in sizes from 1 to 3 nm, are of particular interest due to their unique characteristics that emerge from a substantial increase in undercoordinated surface atoms and the quantization of energy states. These give rise to distinctive properties and enhanced reactivity, distinguishing them from their larger counterparts.[18,19] Precisely controlling the size of the ultra-small Ag revealed the quantum competition between the effects of the metal/matrix interface, and those of electronic spill-out and the substrate.[6] As such, size and shape control remain crucial for the effective application of these nanoparticles.

Among the various synthesis approaches, bottom-up colloidal wet-chemical routes are currently the most effective for achieving uniform nanocrystals with high yields. To date, studies on the wet chemical synthesis of Ag NPs span a wide variety of methods. These include chemical reductions of a silver precursor in organic[20–23] or aqueous phases[24–27], microwave-[28] and photo-assisted reductions,[29,30] seed-mediated synthesis,[31] and modified polyol processes.[32,33] Nanoparticle syntheses involving the reduction of metal salts in aqueous solutions leverage the stability, polarity, and cost-effectiveness of water, and require electrostatic stabilizers to prevent NP aggregation. However, avoiding oxidation of ultra-small Ag NPs in aqueous medium is challenging.[34,35] Alternatively, reducing organometallic precursors in nonpolar media in the presence of surfactants offers enhanced control over particle nucleation and growth due to a tailored reactivity of the precursor facilitated by selective ligand interactions.[36,37] This approach generally requires the preparation of non-commercial precursors and their handling in controlled atmospheres. A third approach, investigated in this study, is the reduction of commercial metal salts in nonpolar media. Using bulky organic ligands that form complexes with the metal ions allows for their complete dissolution. Additionally, the ligands stabilize the final metal nanoparticles sterically, protecting them from aggregation and oxidation. Due to their presence at different stages of NP crystallization, the ligands influence the particle size, morphology, and reaction kinetics by modulating activation energies of nucleation and growth, particularly in diffusion-limited environments.[38,39]

In this later approach, a thorough understanding of the initial solutions is thus crucial, as ionic precursors in nonpolar media can form supramolecular assemblies, which differ significantly from simple ions dissolved in water or organometallic complexes in nonpolar solvents. Previous studies have reported the synthesis of monodisperse 2 nm Au icosahedral nanoparticles thanks

to the reduction of gold(III) chloride clusters in a non-aqueous medium.[40,41] These clusters formed by the simple dissolution of hydrated $HAuCl_4$ in an oleylamine solution in hexane have been suspected of playing a key role in the nucleation stage of gold particles and in controlling their size.

In this paper, we extend this approach to the synthesis of ultra-small Ag NPs through the reduction of silver salts by trialkylsilanes in the presence of oleylamine (OY) in a non-polar solvent. This study aims both to establish a robust method for producing ultra-small silver NPs with precise control of size and structure through different synthesis parameters, and to validate the strategy of starting from a metal precursor in the form of supramolecular clusters. Silver particles were synthesized by varying a large number of parameters, including reagent concentrations (Ag, silane, OY) and temperature over wide ranges, as well as the nature of the silver precursor. Mean size and size distribution of the Ag particles were characterized by *in situ* SAXS and TEM and their atomic structure identified by PDF analysis. A detailed analysis of the silver precursor solution prepared in the different experimental conditions was carried out, revealing the formation in solution of large clusters of $Ag^{(I)}$ complexes prior to the reduction. The classical nucleation mechanism from isolated monomers fails to explain the Ag particle size. Instead, we explore the idea of a confined nucleation occurring within the $Ag^{(I)}$ clusters, suggesting an original pathway for NP formation.

2. Experimental details

2.1 Synthesis of Silver Nanoparticles (Ag NPs)

Silver nitrate ($AgNO_3$, ACS 99.9+% metals basis, Alfa Aesar), silver trifluoroacetate (98%, Thermo Scientific), silver trifluoromethanesulfonate (98%, Thermo Scientific), oleylamine (OY, 89-90%, Thermo Scientific), triethylsilane (TES, 99%, Sigma-Aldrich), triisopropylsilane (TIPS, 98%, Thermo Scientific), hexane (mixed isomers, 98+%, Alfa Aesar), and decane (99%, Thermo Scientific) were used without any further purification.

Silver nanoparticle syntheses were conducted by reducing $AgNO_3$ by TES in a solution of OY in hexane. Batch solutions of 3.0 mL were prepared by mixing 1.5 mL each of a precursor and reducing agent solution, respectively. In a standard reaction, the nominal [Ag] was kept at 0.02 $mol.L^{-1}$, the [OY]/[Ag] was fixed at 2.5 ([OY] = 0.05 $mol.L^{-1}$), and [TES] was fixed at 1 $mol.L^{-1}$. First, the silver precursor solution was prepared by sonicating 10.2 mg of $AgNO_3$ in a solution containing 49.4 µL of OY in 1.45 mL of hexane for 30 minutes at 40°C. Next, a solution containing 479 µL of TES in 1.02 mL of hexane was rapidly injected into the precursor solution, which was maintained at 40°C in a thermostatic bath. Upon injection, the colorless solution rapidly turned yellow, then gradually to dark yellow. The reaction mixture was kept at 40°C for three hours. Complementary reactions were performed following the same protocol, but with higher [Ag], [OY]/[Ag] ratios, and temperature, or with alternative $Ag^{(I)}$ precursors, namely silver trifluoroacetate and silver trifluoromethanesulfonate. For reactions conducted at higher temperatures, an oil bath and Schlenk setup were used. In these cases, the reducing agent

solution was added to the precursor solution at room temperature followed by immediate immersion in the oil bath, where the mixture was held for three hours. Considering the very small relative volume of the reaction solution vs that of the oil bath (3 mL vs many L), it is reasonable to assume that the solution reached the set temperature almost instantaneously. Due to the proximity of their respective boiling points, the solvent was switched to decane for reactions above 60°C, and triisopropylsilane (TIPS) served as the reducing agent instead of TES for reactions above 100°C.

2.2 *In situ* characterization

Small Angle X-Ray Scattering (SAXS)

Ag NP colloidal suspensions were characterized by SAXS using 1.5 mm borosilicate capillaries as sample holders. Measurements were performed on a XEUSS 2.0 laboratory instrument equipped with a pixel detector PILATUS 1M (DECTRIS) and a GeniX3D Cu Kα X-ray micro-source provided by XENOCS (λ = 1.54 Å). The q-range was 0.023 – 1.47 $Å^{-1}$ while acquisition times were around 5 minutes per sample. Further measurements were carried out on the SWING beamline at the SOLEIL synchrotron facilities in Paris, France using a beam energy of 12 keV, a q_{range} of 0.015 – 1.15$Å^{-1}$, and acquisition times of 10 ms. Recorded data were transformed into the absolute scale by using pure hexane as the standard with an absolute scattering intensity of 2.86 x 10^{-2} cm^{-1}. The SAXS data for the Ag NP suspensions were fitted using a polydisperse form factor of spheres with a Schultz distribution[42], providing the mean particle diameter (d_m), polydispersity (PD; defined by the ratio σ/d_m where σ is the standard deviation of the size distribution), and the volume fraction of the spheres. Additional details are provided in Supporting Information (see Fig. S1). For the precursor solutions, the SAXS data were fitted to a Guinier-Porod model, yielding a gyration radius and a Porod exponent (Supporting Information, Fig. S2).

Wide-Angle X-Ray Scattering (WAXS) and Pair Distribution Function (PDF) analysis

WAXS measurements were collected with a lab-based Empyrean III diffractometer used in transmission geometry, with a molybdenum anode source and a Galipix3D detector providing a q_{max} of 16.66$Å^{-1}$. Measurements of the nanoparticle suspensions and the reference were performed separately in 1 mm thick capillaries. The total q range was split into five different sections with increasing variable counting times leading to a total acquisition time of 15h per sample. Complementary measurements were conducted at the ID15A beamline at the ESRF in Grenoble, France, using an X-ray beam energy of 69 keV (λ = 0.1797 Å) and a Pilatus 2M detector with a q-range of 0.25 – 36.7 $Å^{-1}$.

The Pair Distribution Functions (PDFs) were extracted using the application PDFgetX3[43]. Nanoparticle structural models at the atomic scale were performed using an atomic simulation environment (ase) python library[44]. The experimental PDFs were then compared to theoretical PDFs of known similar structures. Least-square refinement of the experimental PDFs was done using the diffpy-cmi package. Further model refinement was subsequently achieved using a reverse Monte Carlo approach using the fullrmc software[45].

Microfluidic experiment for in situ UV-Vis Spectroscopy

To study reaction kinetics with a high temporal resolution, microfluidic reactors were fabricated according to a design previously published for the study of Au NPs syntheses[46], and briefly

described here for completeness. The microreactors consisted of two inlets for the injection of reagent solutions, followed by two pre-mixing channels preceding a main butterfly-type mixer with a 20 μm × 50 μm cross-section. A reaction channel was finally connected to an outlet channel. The mixer and the reaction channel were connected to a bypass channel controlled by a HPLC valve, allowing for the regulation of pressure differentials when switching between continuous flow (short reaction times) and stopped-flow configurations (longer reaction times). A complete schematic can be seen in the Supporting Information (Fig. S3).

Several optical interrogation regions were placed perpendicular to the main reaction channel in the microfluidic reactors. To implement UV-Vis spectroscopy, 220 μm solarization-resistant, pig-tailed multimode fiber optics (Thorlabs, US, N.A. 0.22) were coupled through self-aligning optical channels and connected to a Deuterium–Halogen balanced light source AvaLight-DH-SBAL (Avantes, Netherlands) and an AvaSpec-2048-USB2-RM multichannel spectrometer (Avantes, Netherlands) at their ends. The reduction of $Ag^{(I)}$ to $Ag^{(0)}$ was tracked in the main reaction channel by following the change in absorbance over time at $\lambda = 410$ nm, which was the wavelength at which an emerging plasmon band for the NPs was observed (Fig. S4).

2.4 *Ex situ* characterization

For further characterizations, the synthesized Ag NPs were washed by adding 200 μl of OY and 3 mL of absolute ethanol to 1 mL of the mother liquor solution, and then centrifuged at 11000 rpm for 10 minutes. The NP precipitate was redispersed in a small amount of hexane. A few drops of this nanoparticle suspension were then drop casted onto a silicon substrate and analyzed by XRD and XPS after drying. A single drop of the diluted NP suspensions was added evenly on top of carbon coated grids for TEM observations.

X-Ray Diffraction (XRD)

Classical structural analysis by XRD was performed on a Panalytical Empyrean diffractometer with a Co Kα X-ray source (Kα (Å) = 1.79), a Bragg–Brentano HD primary optics and a linear Pixcel1D detector. The explored 2θ range was 35° – 110°, with a step size of 0.13, and acquisition time of 400 s per step. As the Ag *fcc* reference file used a copper source with a different Kα radiation, experimental and reference XRD measurements were converted to q within a range of 2.25 – 5.75 $Å^{-1}$ for better comparison.

X-Ray Photoelectron Spectroscopy (XPS)

XPS spectra of the Ag NPs were measured using a Thermo Fisher Scientific K-Alpha^{+} X-ray Photoelectron Spectrometer with a monochromatic Al Kα X-ray source (1486.6 eV, 400 μm spot size). The pass energy of the spectrometer was set to 150 eV for the survey scan and 40 eV for high-resolution narrow scans.

Transmission electron microscopy (TEM)

TEM imaging of the Ag NPs was carried out with a JEOL JEM 1400 ORIUS microscope. A number-weighted size distribution was generated by analysing approximately 200 nanoparticles using the ImageJ software.

3. Results and discussion

3.1. Particle Size Distribution

The influence of three parameters, TES concentration, Ag concentration, and temperature, on the particle size distribution was studied first (Fig. 1). The mean particle size, polydispersity, and yield of reduction from the SAXS analysis are summarized in Table 1.

3.1.1 Influence of the concentration of TES

In a first set of experiments [Ag] and the ratio [OY]/[Ag] were kept constant at 0.02 mol.L^{-1} and 2.5, while the concentration of [TES] was varied from 0.01 mol.L^{-1} to a large excess of 1 mol.L^{-1}. All reactions were carried out at 40°C. The colourless precursor solution turned yellow and then dark yellow upon the addition of TES, with a gradual colour change over several minutes at low concentrations of [TES] to an almost instantaneous colour change at higher concentrations. After 3 hours of reaction, the NP suspension prepared using 0.01 mol.L^{-1} TES was lighter and more translucent than the ones prepared with higher concentrations of TES, indicating differences in the reduction yield. The SAXS profiles of the Ag NP suspensions are shown in Figure 1a. All curves were well fitted with a single population of Ag spheres.

The mean particle size remained constant regardless of [TES] with a mean size of approximately 2.85 nm (Tab. 1). However, as [TES] was increased from 0.01 mol.L^{-1} to 1 mol.L^{-1}, the gradual sharpening of the slope and the appearance of distinct oscillations at higher q values indicated a decrease in Ag NP polydispersity from 16% to 9% (Tab. 1). A representative TEM image of Ag NPs synthesized with a TES concentration of 1 mol.L^{-1} is shown Figure 1d. Image analysis gave a mean particle diameter of 2.85 nm and a polydispersity of 14%, which is in excellent agreement with the SAXS results. The reaction yield inferred from the SAXS analysis was 59% with a [TES] = 0.01 mol.L^{-1}, and it increased with higher [TES] reaching a maximum yield of 100% at [TES] $\geq$ 0.04 mol.L^{-1} (Tab. S1). This trend is reflected in the scattering intensity at low q values, which increases with [TES] up to 0.04 mol.L^{-1}, at which point it stabilizes. A [TES]/[Ag] ratio of 0.5 was expected to satisfy the stoichiometry of the reduction of $Ag^{(I)}$ to $Ag^{(0)}$ with TES, as TES formally acts as a hydride donor, capable of releasing two electrons. Nevertheless, experimentally, 2 equivalents of TES (i.e. 0.04 mol.L^{-1}) were required to complete the reduction after 3 hours of reaction. In the other experiments [TES] was fixed at 1M.

3.1.2 Influence of the concentration of the precursor

In a second set of experiments, the concentration of $AgNO_3$ was varied from 0.01 mol.L^{-1} to 0.16 mol.L^{-1}, while maintaining a constant [OY]/[Ag] ratio of 2.5, and a large excess of TES (1 mol. L^{-1}). The resulting SAXS profiles are shown in Figure 1b. The scattering intensity at low q increased with [Ag] concentration due to the higher number density and volume fraction of NPs. Reaction yield remained close to 100% for all initial [Ag] concentrations, consistent with the large excess of TES used. Fitting of the data revealed that the Ag NPs size increased by nearly 10% from 2.84 nm at [Ag] = 0.01 mol.L^{-1}, to 3.1 nm at [Ag] = 0.16 mol.L^{-1}. In all cases, the particles were highly monodisperse, with polydispersity decreasing when [Ag] was increased. For [Ag] = 0.16 mol.L^{-1}, the nanoparticles exhibited very low polydispersity of only 6%. Increasing the Ag concentration did not lead to particle coalescence, but on the contrary significantly reduced NP polydispersity.

3.1.3 Influence of temperature

In a third set of experiments, [Ag], [OY] and [TES] concentrations were fixed to 0.02 mol.L^{-1}, 0.05 mol.L^{-1} and 1 mol.L^{-1}, respectively, while the temperature was varied from 25°C to 120°C. Hexane was used as solvent for temperatures below 60°C and decane for temperatures above. The corresponding SAXS profiles of the Ag NP suspensions are shown in Fig. 1c. The reaction temperature had minimal impact on the size of the nanoparticles. The scattering curves were nearly identical across all syntheses (Fig. 1c) providing 100 % reaction yield, low polydispersity and a mean particle diameter ranging from 2.7 to 2.9 nm (Tab. S1). At 120°C, the oscillations at high-*q* slightly dampened, indicating an increase in polydispersity to 16%.

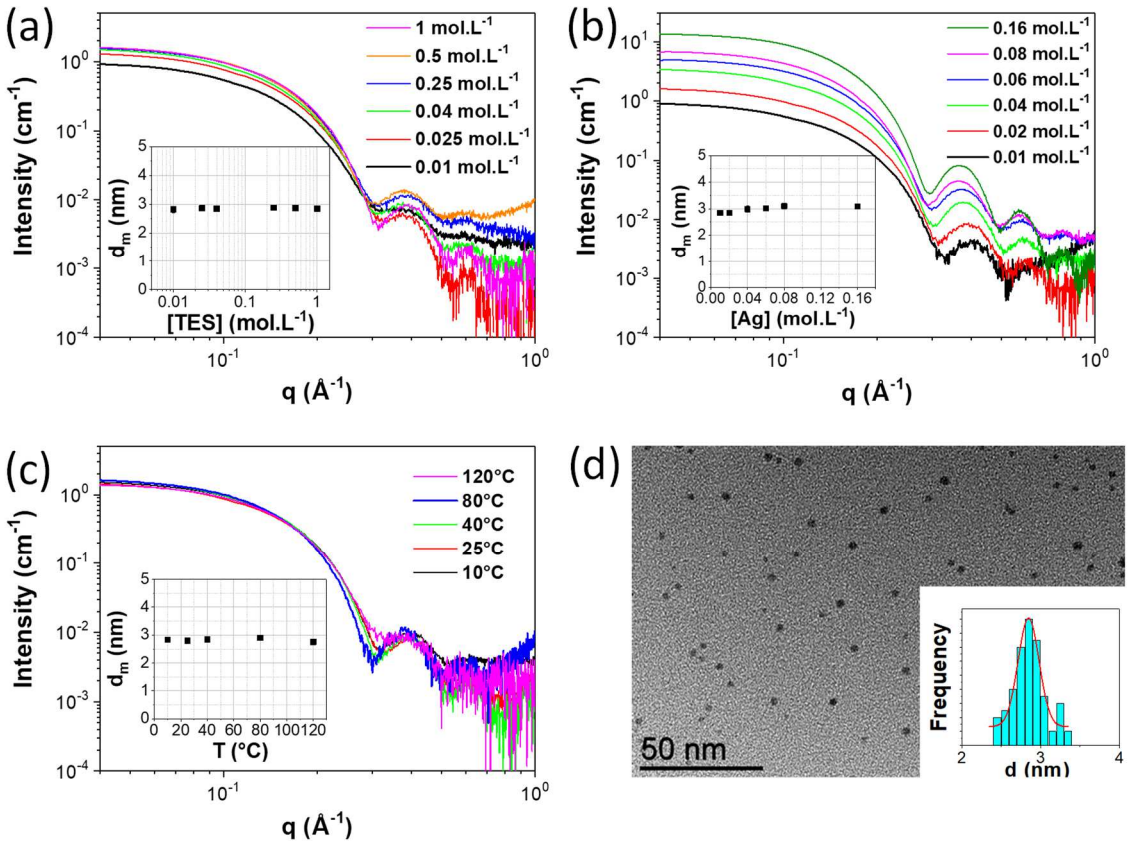

Figure 1. SAXS profiles of Ag NP suspensions prepared by the reduction of $AgNO_3$ with TES dissolved in a solution of OY in hexane (a) for [TES] varying in the range 0.01 to 1 mol.L^{-1} ([Ag], [OY]/[Ag] and T were fixed at 0.02 mol.L^{-1}, 2.5 and 40 °C, respectively); (b) for [Ag] varying in the range 0.01 to 0.16 mol.L^{-1} ([TES], [OY]/[Ag] and T were fixed at 1 mol.L^{-1}, 2.5 and 40 °C, respectively); (c) for T varying in the range 10°C to 120°C ([Ag], [TES] and [OY]/[Ag] were fixed at 0.02 mol.L^{-1}, 1 mol.L^{-1} and 2.5, respectively) ; (d) TEM image and size distribution (inset) of Ag NPs prepared at 40 °C with [Ag] = 0.02 mol. L^{-1}, [TES] = 1 mol. L^{-1} and [OY]/[Ag] = 2.5.

Table 1. Summary of the SAXS fitting results using a Schultz distribution for Ag NPs synthesized under various reaction conditions. The table includes the mean particle diameter (d_m), polydispersity defined by the ratio σ/d_m where σ is the standard deviation, and reaction yield (calculated as the percentage ratio of final to nominal [Ag] concentration). [a] [Ag] = 0.02 mol.L^{-1}, T = 40°C, [OY]/[Ag]= 2.5; [b] [TES] = 1 mol.L^{-1}, T = 40°C, [OY]/[Ag]= 2.5; [c] reactions carried out in hexane until 40°C and in decane until 120°C, [Ag] = 0.02 mol.L^{-1}, [TES] = 1 mol.L^{-1}, [OY]/[Ag] = 2.5; [d] [Ag]= 0.02 mol.L^{-1}, [TES] = 1 mol.L^{-1}, T = 40°C.

Experimental Conditions		***d_m (nm)***	***σ/d_m***	***Yield (%)***
[TES] (mol.L^{-1})[a]	0.010	2.8	0.16	59
	0.025	2.85	0.14	79
	0.040	2.85	0.12	93
	0.25	2.9	0.11	100
	0.5	2.9	0.10	100
	1	2.85	0.09	100
[Ag] (mol.L^{-1})[b]	0.01	2.85	0.10	100
	0.04	3.0	0.08	100
	0.06	3.0	0.08	100
	0.08	3.1	0.07	100
	0.16	3.1	0.06	100
Temperature (°C)[c]	10	2.8	0.11	100
	25	2.8	0.11	100
	80	2.9	0.08	100
	120	2.8	0.14	100
[OY]/[Ag][d]	5	2.65	0.09	100
	10	2.4	0.09	100
	15	2.3	0.10	100
	20	2.2	0.10	100

3.2. Structural Analysis of the Ag NPs

The XRD patterns of Ag NPs prepared with different starting Ag concentration are shown in Figure 2 and the ones obtained with different TES concentration and at different temperatures are given in supplementary materials (Fig. S5). In all cases, a main diffraction peak was observed at the constant value q = 2.76 Å^{-1} with a less intense shoulder peak also at a constant value of q = 3.10 Å^{-1}. Compared to the *fcc* crystalline structure of bulk Ag (Reference JCPDS file N° 04-0783), the main peak was noticeably shifted to higher q values with respect to the {111} reflection expected at q = 2.66 Å^{-1}. The full width at half maximum (FWHM) value of the main peak was approximately 0.26 Å^{-1}. In 2θ scale this broadening corresponds to a FWHM of 4.5 degrees which is a very large value, typical of crystallites of very small size.

No significant structural changes were observed as a function of [Ag], [TES] and temperature (Fig. S5), with the peak positions and the FWHM remaining constant.

To further describe the atomic structure in detail, *in-situ* HE-XRD patterns of Ag NPs were recorded across a wide *q*-range, and atomic Pair Distribution Functions (PDF) were calculated. Figure 3 shows a representative experimental PDF and the comparison with structural models. The first peak of the PDF at 2.87 Å corresponds to the Ag-Ag interatomic distance, which is slightly shorter than the Ag-Ag bond length of 2.89 Å in bulk fcc silver (JCPDS file N° 04-0783). [47] This inter-atomic distance contraction is however smaller than that observed in thiol-passivated silver clusters.[48] The extension of the G(r) oscillations in the r-space to 2.7 nm is in good agreement with the mean size of 3.1 nm determined by SAXS. The minor differences could be indicative of a small degree of positional disorder on the last atomic shell at the Ag NP surface. The experimental PDFs of the Ag NPs were then compared with the theoretical PDFs of different models of similar size: a cuboctahedron with a *fcc* structure containing 923 atoms, a decahedron of 818 atoms, and an icosahedron of 923 atoms. The interatomic distances in the theoretical models were let free to best fit the experimental PDFs. The *fcc* and decahedral models show clear discrepancies, particularly in the mid- and high-r zones, while there is a strong correlation with the icosahedral model, especially in the position and relative intensities of the doublet peaks at r = 4.96 Å and 5.56 Å. To achieve an even closer match with the experimental data, a distorted icosahedral model was built by allowing all atoms to displace from their ideal positions in the 923-atom perfect icosahedron. Using the FULLRMC software, the best fit was obtained by introducing a moderate degree of local structural disorder. The computed PDFs of said distorted icosahedron closely matched the experimental PDFs in fine detail (Fig. 4).

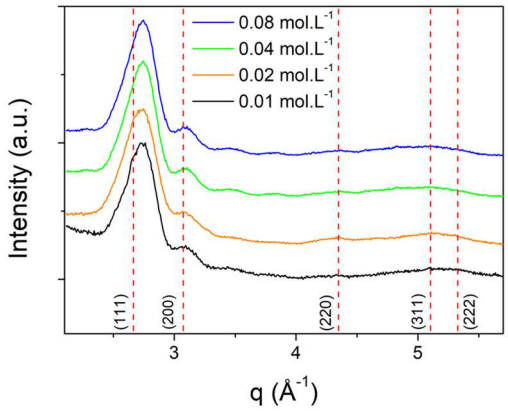

Figure 2: XRD patterns of Ag NPs prepared with different concentrations of Ag ([TES] = 1 mol.L^{-1}, [OY]/[Ag] = 2.5 were kept constant). ($q = \frac{4\pi sin\theta}{\lambda}$, $\lambda_{K\alpha}$(Co) = 1.790Å). Dash red lines are the expected q values of the fcc Ag reflections (from JCPDS file N°04-0783).

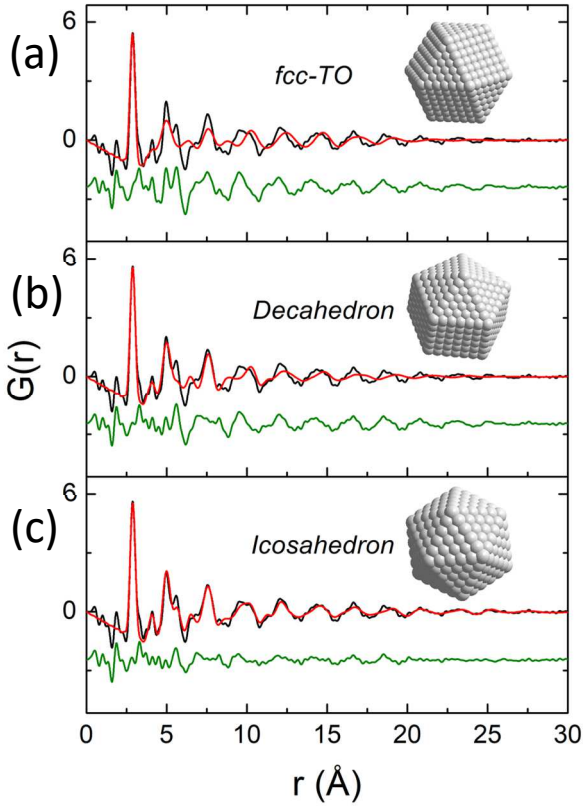

Figure 3. Experimental PDFs (black) of Ag NPs with mean size of 3.1 nm prepared by the reduction of $AgNO_3$ ([Ag] = 0.08 mol.L^{-1}) with [TES] = 1 mol.L^{-1} at 40 °C and [OY]/[Ag] = 2.5, compared with computed PDFs (red) of (a) a 923-atom cuboctahedron with *fcc* structure, (b) a 818-atom decahedron, and (c) an 923-atom icosahedron, represented as insets. The green lines represent the differences between the experimental PDFs and the fits – vertically shifted for better visualization

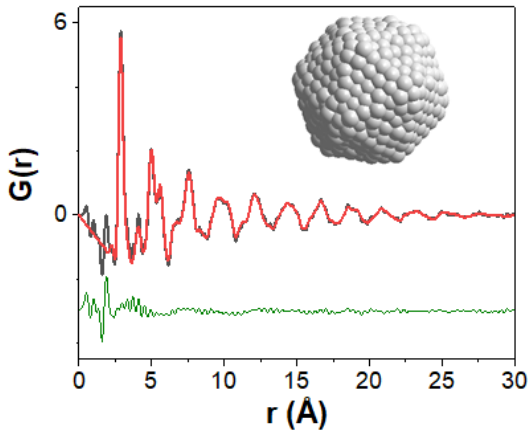

Figure 4. Comparison between the experimental PDF of 3.1 nm mean diameter Ag NPs (black) and the computed PDF of a 923-atm distorted icosahedron model (red). The green line represents the difference between experimental PDF and fit.

While the metallic nature of the Ag NPs was confirmed through PDF analysis, their surface coordination chemistry was examined via XPS analysis. Following a washing process to remove the most of the excess OY and TES, the XPS survey scan revealed binding energies for Ag 3d and 3p, as well as C 1s and N 1s. The Ag $3d_{5/2}$ peak was observed at 368.2 eV (Fig. S6). The N1s XPS spectrum displayed two contributions with a main peak (74% of the total N 1s intensity) centered at 399 eV corresponding to free OY and a smaller peak at 400.5 eV that can be attributed to N atoms of OY coordinated to Ag NP surface[49] (26% of the total N 1s intensity) (Fig. S6).

3.3. Comparison with the classical nucleation theory

Classical models of nucleation and growth in the liquid-phase synthesis of inorganic nanoparticles describe a process in which atomic nuclei have to reach a critical size to overcome the energy barrier related to the competition between the free energies of the bulk and the newly emerging interface[50,51]. These nuclei subsequently grow through atom-by-atom additions. The formation of monodisperse nanoparticles is generally explained by the LaMer model, which requires a distinct separation between the nucleation and growth stages. This can be verified if the nucleation step rapidly consumes a large proportion of the monomers formed in solution, whose concentration falls below the supersaturation threshold, thereby leading to growth. Once nucleated in a short burst, the particles grow at the same rate, resulting in uniform final particle size. According to this model, the final size, polydispersity, and number density of the particles are highly dependent on the monomer supply rate (i.e. reaction rate)[52–54]. In the classical nucleation approach, the critical size (r^*) of the initial nuclei is given by the equation:

$$r^* = \frac{2\Omega\alpha}{\Delta\mu} = \frac{2\Omega\alpha}{k_B T ln S} \quad (1)$$

where $\Delta\mu$ is the difference in chemical potential, Ω is the molecular volume, α is the interfacial energy, k_B is the Boltzmann constant, T the temperature, and $S = \frac{C}{C_0}$ the supersaturation, with C and C_0 are the concentration and solubility of the monomers. Several computational studies involving nucleation and either diffusion-limited or surface reaction-limited growth steps have precisely described the effect of initial supersaturation and temperature on nucleation rate, final particle size and polydispersity. In the framework of classical nucleation theory, these studies go far beyond a simple examination of Eq. 1.[55,56] However, what is generally predicted is that high initial supersaturation increases the nucleation rate, decreases the growth rate and favours small NPs.[55] The same effect is expected with increasing the temperature – favouring a decrease in mean particle size and its polydispersity.[55] In case of a higher activation energy of the growth step compared to the chemical reduction that provides the monomers, Förster and co-workers showed that increasing temperature can favour the growth over the nucleation leading to bigger particles.[56] This observation remains, however, within the framework of the classical nucleation theory.

What distinguishes the nanoparticle synthesis presented here from others previously described in the literature is that the size of the silver particles remain largely unaffected by most of the parameters studied. For example, Peng et al.[57] developed a similar organic phase synthesis of monodisperse Au NPs in which OY was used as the surfactant, with *tert*-butylamine-borane complex (TBAB) as the reducing agent and tetralin as the solvent. The authors observed that

varying the reaction temperatures from 2°C to 40°C helped to significantly fine-tune the average particle sizes from 9.5 nm to 2.4 nm. The authors proposed a mechanism of formation that followed a burst nucleation commonly seen in the LaMer model, with a strong effect of temperature on nucleation rate, as expected with the classical nucleation theory. In contrast, in this work, raising the reaction temperature over a wide range (wider than the range in ref. 57), had almost no effect on the particle size and the icosahedral structure. The same absence of effect was observed when Ag and TES concentrations were increased. Both concentrations are expected to increase significantly the initial supersaturation. The absence of size variation as a function of initial [Ag] concentration seems also contradictory to a classical nucleation mechanism, since a higher concentration of metal salts and reducing agent should accelerate the reaction rate, allowing a higher supersaturation rate to be reached, resulting in a higher nucleation rate and smaller final particles.[55]

All the parameters that have a significant effect on the reaction rate also have generally a significant effect on the final particle size,[56] which is a notable difference from our study. In order to illustrate the absence of a relation between final particle size and reaction rates, the effect of [TES] on the rate of $Ag^{(0)}$ formation was investigated by *in situ* time resolved UV-Vis experiments. For this purpose, a photonic-lab-on-chip approach was used, and UV-Vis spectroscopy was coupled to a microfluidic setup as described in the experimental section. The reduction of $Ag^{(I)}$ to $Ag^{(0)}$ was monitored in a main microfluidic reactor channel by means of in-plane perpendicular optical interrogation channels, by tracking the absorbance at the wavelength corresponding to the maximum of the plasmonic peak of the Ag NPs (λ = 410 nm, Fig. S4). Figure 5a shows the variation in absorbance over time for reactions with TES concentrations of 0.01, 0.06, and 1 $mol.L^{-1}$, while keeping the other parameters constant ([Ag] = 0.02 $mol.L^{-1}$, [OY]/[Ag] = 2.5, T = 40°C). As expected, the absorbance increased at different rates depending on [TES]. The initial reaction rate (*d(Abs)/dt*, Fig. 5b) was determined from the initial slope of the curves and found to be linearly dependent on the TES concentration (inset, Fig. 5b), indicating a first-order reaction with respect to TES. Thus, despite the reaction rate varying over two orders of magnitude by adjusting TES concentration, the final particle size remained constant at around 2.85 nm.

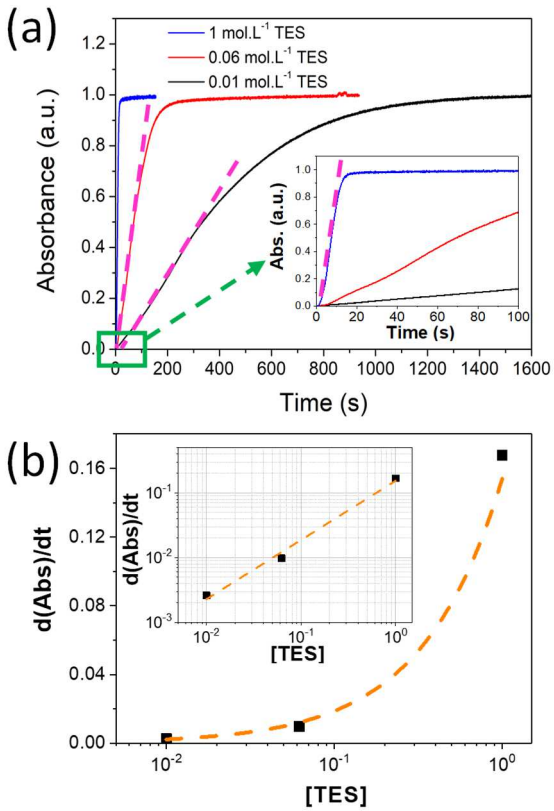

Figure 5. (a) Time-resolved absorbance measurements following the reduction of $AgNO_3$ by TES = 0.01 (black), 0.06 (red), and 1 (blue) mol.L^{-1} in a solution of hexane and OY ([Ag] = 0.02 mol.L^{-1}, [OY]/[Ag] = 2.5, T = 40°C). Inset shows a zoom at shorter reaction times. Final absorbance plateaus were normalized to 1 due to differences between the curves as a result of minor defects in the optical paths between different microreactors (slight channel deformations due to manual fabrication); (b) rate of reaction determined by taking the slope of the nucleation stage (change in absorbance over time) as a function of [TES] (log-log scale as inset).

3.4. The role of the initial $Ag^{(I)}$ clusters

Several studies of nucleation mechanisms in the liquid-phase synthesis of inorganic nanoparticles have shown that the energy landscapes can be more complex than the single energy barrier described in the classical model. These processes can involve multiple activation barriers or intermediate metastable states, which play crucial roles in the formation of the final nanoparticles.[58] In the following section, we explore this possibility by paying a closer attention to the precursor solutions.

The first step in the formation of the Ag NPs was the dissolution of $AgNO_3$ in a solution of OY in hexane, forming a colourless solution of a complex between $AgNO_3$ and OY. To gain a deeper understanding of the processes involved in the formation of the Ag NPs, the precursor solutions before the addition of TES were examined using SAXS, at different temperatures and for different [Ag]. Figure 6a shows the scattering profiles at different temperatures of the precursor solution in hexane with [Ag] = 0.02 mol.L^{-1} and [OY]/[Ag] = 2.5. In all cases, a

scattering intensity was observed, with a Guinier plateau in the low-*q* region and a Porod regime in the high-*q* region. Since no Ag NPs had been formed at this stage, and the scattering length density (SLD) of OY and hexane cannot be distinguished, the scattering intensity must have arisen from the presence in solution of supramolecular assemblies of Ag ions which exhibit a strong electronic density contrast with the solvent. The empirical chemical formula $\{Ag^{(I)} - OY - NO_3^-\}_n$ can be suggested and for simplicity, these assemblies will be referred as $Ag^{(I)}$ clusters from this point on. Such kind of clusters were also observed after dissolution of $HAuCl_4$ in solution of OY in hexane.[40] The scattering profiles of the $Ag^{(I)}$ clusters were analyzed using a Guinier-Porod model in SasView (see details in *Supporting Information*). The diameter of the clusters, determined using the SAXS profile at 40 °C, was found to be 3.05 nm (R_g = 1.18 nm) with a Porod exponent of 3.67, indicating a surface fractal conformation. The scattering curves showed minimal change with increasing temperature (Fig. 6a), indicating that the clusters do not dissociate and their size is unchanged at high temperature (Tab. 2).

The SAXS patterns of $Ag^{(I)}$ clusters prepared with various Ag concentrations (while keeping the OY/Ag molar ratio fixed at 2.5) are shown in Figure 6b-c. When [Ag] was increased, the SAXS intensity increased in agreement with an increasing number density of $Ag^{(I)}$ clusters but no significant change in the cluster size was observed (Tab. 2). In addition, for [Ag] > 0.04 $mol.L^{-1}$, a broad peak emerged in the mid-*q* region of the SAXS pattern, shifting slightly to higher *q* with increasing [Ag] (Fig. 6c). This is characteristic of the emergence of a structure factor arising from repulsive interactions between the $Ag^{(I)}$ clusters. The peak position, centred around 0.14 $Å^{-1}$, corresponds to an average correlation distance of 4.4 nm between the $Ag^{(I)}$ clusters in solution, indicating a very high-volume fraction and thus a strong repulsion between the $Ag^{(I)}$ clusters.

In conclusion, the temperature and silver concentration shown to have no effect on final NP size also have no effect on the size of $Ag^{(I)}$ clusters present in the precursor solution. This suggests that while the final NP size does not correlate with the reaction rate, it is directly influenced by the size of the $Ag^{(I)}$ clusters. Moreover, it was shown that polydispersity decreased with increasing [Ag], while the final NP size remained constant. The repulsion between the clusters likely prevented aggregation of initial seeds, favouring low polydispersity of the final particles. It seems again in favour of a nucleation occurring within the $Ag^{(I)}$ clusters.

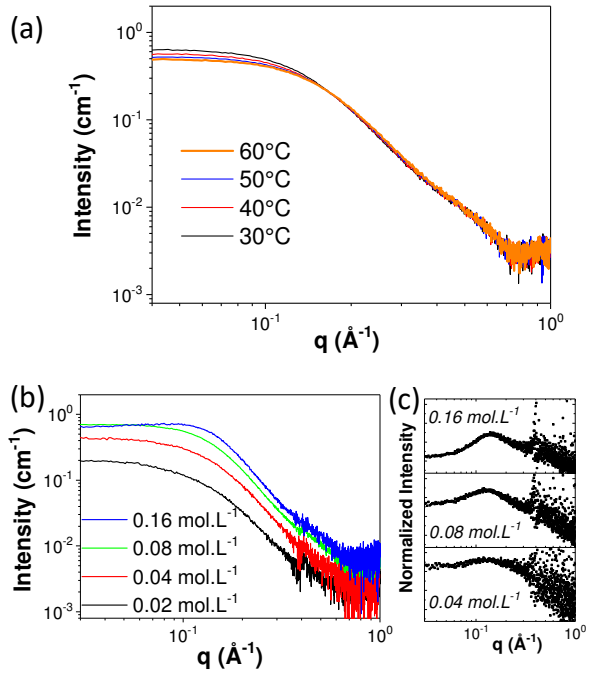

Figure 6. (a) SAXS profiles of $Ag^{(I)}$ clusters measured at different temperatures in hexane ([Ag] = 0.02 mol.L^{-1} and [OY]/[Ag] = 2.5); (b) SAXS profiles of $Ag^{(I)}$ clusters formed with different concentrations of Ag ([OY]/[Ag] = 2.5 was kept constant); (c) SAXS curves of figure 6(b) normalized by the curve at [Ag] = 0.02 mol.L^{-1} to better visualize the emerging peak of the structure factor.

In order to validate this hypothesis, two additional parameters were varied with the aim to vary the $Ag^{(I)}$ cluster size and to examine the consequence on the final Ag NP size.

The $Ag^{(I)}$ clustering likely results from a balance between ionic interactions between Ag^+ and NO_3^-, covalent complexation of Ag^+ by OY, and Van der Waals interactions between the long alkyl chain of OY coordinated to Ag and hexane. In order to modify the balance of interactions, the effect of [OY] and the nature of the silver precursor were varied. As the [OY]/[Ag] ratio increased from 2.5 to 20, a reduction in scattering intensity at low *q* and a shift of the 'knee' position to higher *q* values were observed (Fig. 7a), resulting in a decrease in the cluster size to a mean diameter of 2.4 nm (Tab.2). Changing the counter anion could modify the ionic balance in the clustering of the $Ag^{(I)}$ ions, providing an alternative approach to control the size of the clusters. SAXS analysis of the precursor solutions using silver trifluoroacetate and silver trifluoromethanesulfonate ([OY]/[Ag] =2.5) confirmed the presence of similar $Ag^{(I)}$ clusters, but with smaller sizes compared to those formed with $AgNO_3$ (Fig. 7b). Guinier-Porod model fitting indicated that the clusters formed with these two precursors were approximately 2 nm in size, with a Porod exponent of 2.6 suggesting a transition to mass fractal conformations (Tab. 2).

Ag NPs were subsequently synthesized from these precursor solutions using a large excess of TES to ensure a complete reduction of $Ag^{(I)}$. All reactions were performed at 40°C, with [Ag] and [TES] fixed at 0.02 mol.L^{-1} and 1 mol.L^{-1}. In all cases, SAXS fitting revealed 100% yield. The SAXS profiles of the suspensions prepared with different [OY]/[Ag] ratios are shown in

Figure S7. As the concentration of [OY] increased, the scattering intensity at low *q* decreased, and the "knee" position in the SAXS curve shifted noticeably to higher *q*, indicating a significant reduction in particle size. The fitted mean diameter decreased from 2.85 for the reference experiment ([OY]/[Ag] = 2.5) to 2.2 nm at [OY]/[Ag] = 20 (Tab. 1). Both reduction of silver trifluoroacetate and silver trifluoromethanesulfonate produced also much smaller particles compared to the ones prepared from silver nitrate. SAXS revealed a mean diameter of 1.3 nm, albeit significantly less monodisperse, requiring multiple size populations to fit the SAXS patterns (Fig. S8). Interestingly, a large excess of OY accelerates the dissolution of $AgNO_3$, and slows down the reduction by TES. The colour of the suspension changed more slowly, taking a few seconds, compared to the nearly instantaneous darkening of the solution when using 2.5 equivalents of OY. Thus, a large excess of OY stabilizes the $Ag^{(I)}$ species but at the same time decreases the final particle size. Again, these observations seem contradictory within the framework of classical nucleation mechanism.

Thus, the hypothesis that the final NP size could be controlled by the initial size of the $Ag^{(I)}$ clusters was validated. Based on these experimental observations, it is reasonable to propose that the initial nuclei form confined within these clusters, rather than from the progressive association/dissociation of free $Ag^{(0)}$ atoms in solution. The high local densities of $Ag^{(I)}$ ions within the clusters make them the actual precursor of the metal nuclei. Smaller clusters of precursors resulted in higher number densities, leading to a greater number of nuclei and consequently smaller final particle sizes. According to that, the very first growth step could result from a fast aggregation of silver atoms formed within a cluster of precursors. In this case, the classic nucleation concept may no longer apply. In addition, the particle size may also be influenced by the stable, close-packed "magic-number" configurations that are characteristic of icosahedral motifs.[59]

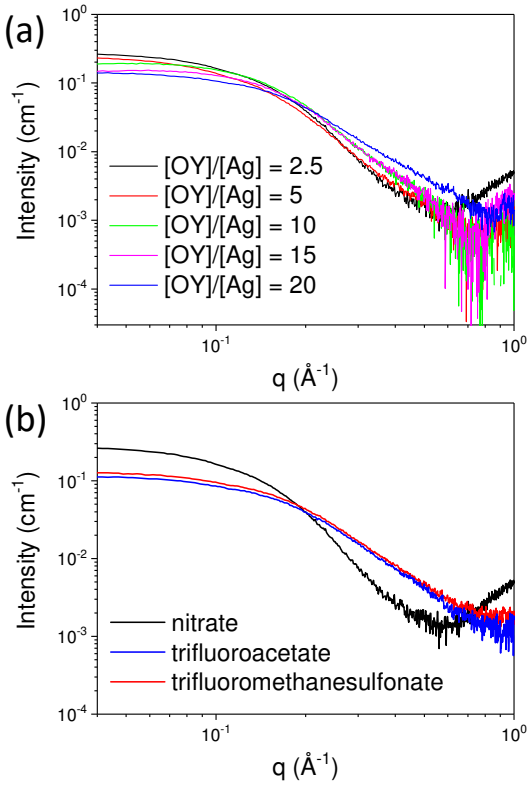

Figure 7. (a) SAXS of $Ag^{(I)}$ clusters formed with different ratios [OY]/[Ag] ([Ag] = 0.02 mol.L^{-1} and T = 40 °C) ; (b) SAXS of $Ag^{(I)}$ clusters formed with different silver precursors, silver nitrate, silver trifluoroacetate and silver trifluoromethanesulfonate ([Ag] = 0.02 mol.L^{-1} , [OY]/[Ag] = 2.5 and T = 40 °C).

Table 2. Summary of the fitting of the SAXS results for the $Ag^{(I)}$ clusters prepared by dissolving $AgNO_3$ and OY in decane under a variety of conditions, including the radius of gyration (R_g), mean particle diameter (d_m), and the porod exponent. [a] [OY]/[Ag]= 2.5, T = 40°C ; [b] [Ag] = 0.02 mol.L^{-1}, [OY]/[Ag] = 2.5 ; [c] [Ag] = 0.02 mol.L^{-1}, T = 40°C; [d] Ag-trifluoromethanesulfonate (Trif), Ag-trifluoroacetate (TrifAce), [Ag] = 0.02 mol.L^{-1}, [OY]/[Ag] = 2.5, T = 40°C.

Experimental Conditions		***R_g (Å)***	***d_m (nm)***	***Porod Exp***
[Nominal Ag] (mol.L^{-1})[a]	0.020	11.8	3.05	3.47
	0.040	11.9	3.1	3.67
Temperature (°C)[b]	30	11.5	2.95	3.36
	50	10.8	2.8	3.31
	60	10.5	2.7	3.30
[OY]/[Ag][c]	5	11.5	2.95	3.61
	10	10.7	2.75	3.49
	15	10.1	2.6	3.38
	20	9.25	2.4	2.97
Ag Precursor[d]	Trif	8.0	2.05	2.64
	TrifAce	8.1	2.1	2.57

4. Conclusion

This study presents a straightforward and reproducible protocol for synthesizing highly monodisperse ultra-small icosahedral Ag NPs, from 2.2 to 3 nm in diameter, with excellent structural homogeneity. From an application perspective, increasing the silver concentration nearly tenfold (from 0.02 mol.L^{-1} to 0.16 mol.L^{-1}) maintains a very high yield of monodisperse NPs, demonstrating significant potential for scalability in industrial contexts. Furthermore, these icosahedral Ag NPs exhibit strong stability across a wide temperature range, remaining intact up to a reaction temperature of 120°C.

From a mechanistic viewpoint, the findings presented here suggest that the nucleation of silver particles deviates from the classical mechanism. Specifically, the final NP size remains unaffected by variations in Ag and reducing agent concentrations or temperature even when these parameters are varied significantly, which suggests that the number of seeds is independent of initial supersaturation and temperature. The analysis of the precursor solution has revealed the formation of $\{Ag^{(I)} - OY - X\}_n$ clusters whose size varies with [OY] and the nature of the silver counter ion (X^-) but is independent of the silver concentration and temperature. The size of these $Ag^{(I)}$ clusters and the repulsive interactions between them play a pivotal role in defining the size and polydispersity of the final Ag NPs, supporting the hypothesis that Ag nucleation occurs confined within these clusters. Future *in situ* time resolved SAXS experiments would provide valuable insights into the transformation process of the $Ag^{(I)}$ clusters into metal NPs. This study provides a nice example of metal NPs synthesis involving the reduction of metal ion clusters, formed by the dissolution of a metal salt in an organic solvent, facilitated by complexation with oleylamine. Extending this approach to other metal salts and reducing agents will be the next step in broadening the scope of this synthesis route.

Associated contents

Supporting information: I. Models for the SAXS analysis of the final Ag NPs and the initial $Ag^{(I)}$ clusters. II. Description of a microfluidic set-up used for the kinetic studies. III. Additional data on nanoparticle characterization. IV. SAXS of Ag nanoparticles using different experimental conditions

Authors information

Corresponding authors

*E-mail: guillaume.viau@insa-toulouse.fr

*E-mail: sebastien.teychene@toulouse-inp.fr

Acknowledgements

This project has received funding from the French ANR competitive national call (Projet NIMRod ANR-21-CE09-0019-01). R.P. thanks the EUR NanoX, n° ANR-17-EURE-0009, for funding for the HERCULES school. SAXS experiments were performed on beamline SWING

at the French synchrotron Soleil proposal (proposal number: 20220441). Thomas Bizien and Javier Perez are warmly thanked for their assistance provided for the use of the beam line. XRD experiments were performed on beamline ID15A at the European Synchrotron Radiation Facility (ESRF), Grenoble, France, proposal CH-6071. Stefano Checchia is warmly thanked for his assistance provided for the use of the beam line.

References

(1) Wang, H.; Zhou, S.; Gilroy, K. D.; Cai, Z.; Xia, Y. Icosahedral Nanocrystals of Noble Metals: Synthesis and Applications. *Nano Today* **2017**, *15*, 121–144. https://doi.org/10.1016/j.nantod.2017.06.011.

(2) Shan, S.; Luo, J.; Kang, N.; Wu, J.; Zhao, W.; Cronk, H.; Zhao, Y.; Skeete, Z.; Li, J.; Joseph, P.; Yan, S.; Zhong, C.-J. Metallic Nanoparticles for Catalysis Applications. In *Modeling, Characterization, and Production of Nanomaterials*; Elsevier, 2015; pp 253–288. https://doi.org/10.1016/B978-1-78242-228-0.00010-7.

(3) Ndolomingo, M. J.; Bingwa, N.; Meijboom, R. Review of Supported Metal Nanoparticles: Synthesis Methodologies, Advantages and Application as Catalysts. *J. Mater. Sci.* **2020**, *55* (15), 6195–6241. https://doi.org/10.1007/s10853-020-04415-x.

(4) Paramasivam, G.; Kayambu, N.; Rabel, A. M.; Sundramoorthy, A. K.; Sundaramurthy, A. Anisotropic Noble Metal Nanoparticles: Synthesis, Surface Functionalization and Applications in Biosensing, Bioimaging, Drug Delivery and Theranostics. *Acta Biomater.* **2017**, *49*, 45–65. https://doi.org/10.1016/j.actbio.2016.11.066.

(5) Gołuński, G.; Konkel, K.; Galikowska-Bogut, B.; Bełdzińska, P.; Bury, K.; Zakrzewski, M.; Butowska, K.; Sądej, R.; Piosik, J. Author Correction: Influence of Silver Nanoparticles' Size on Their Direct Interactions with Doxorubicin and Its Biological Effects. *Sci. Rep.* **2024**, *14* (1), 24050. https://doi.org/10.1038/s41598-024-75135-4.

(6) Campos, A.; Troc, N.; Cottancin, E.; Pellarin, M.; Weissker, H.-C.; Lermé, J.; Kociak, M.; Hillenkamp, M. Plasmonic Quantum Size Effects in Silver Nanoparticles Are Dominated by Interfaces and Local Environments. *Nat. Phys.* **2019**, *15* (3), 275–280. https://doi.org/10.1038/s41567-018-0345-z.

(7) Yan, Z.; Shah, R. A.; Chado, G.; Gray, S. K.; Pelton, M.; Scherer, N. F. Guiding Spatial Arrangements of Silver Nanoparticles by Optical Binding Interactions in Shaped Light Fields. *ACS Nano* **2013**, *7* (2), 1790–1802. https://doi.org/10.1021/nn3059407.

(8) Volokh, M.; Mokari, T. Metal/Semiconductor Interfaces in Nanoscale Objects: Synthesis, Emerging Properties and Applications of Hybrid Nanostructures. *Nanoscale Adv.* **2020**, *2* (3), 930–961. https://doi.org/10.1039/C9NA00729F.

(9) Wei, H. Plasmonic Silver Nanoparticles for Energy and Optoelectronic Applications. In *Ceramic Transactions Series*; Lu, K., Manjooran, N., Radovic, M., Medvedovski, E., Olevsky, E. A., Li, C., Singh, G., Chopra, N., Pickrell, G., Eds.; Wiley, 2011; Vol. 229, pp 171–184. https://doi.org/10.1002/9781118144602.ch17.

(10) Park, M.; Im, J.; Shin, M.; Min, Y.; Park, J.; Cho, H.; Park, S.; Shim, M.-B.; Jeon, S.; Chung, D.-Y.; Bae, J.; Park, J.; Jeong, U.; Kim, K. Highly Stretchable Electric Circuits from a Composite Material of Silver Nanoparticles and Elastomeric Fibres. *Nat. Nanotechnol.* **2012**, *7* (12), 803–809. https://doi.org/10.1038/nnano.2012.206.

(11) Jin, J.-C.; Wu, X.-J.; Xu, J.; Wang, B.-B.; Jiang, F.-L.; Liu, Y. Ultrasmall Silver Nanoclusters: Highly Efficient Antibacterial Activity and Their Mechanisms. *Biomater. Sci.* **2017**, *5* (2), 247–257. https://doi.org/10.1039/C6BM00717A.

(12) Yin, I. X.; Zhang, J.; Zhao, I. S.; Mei, M. L.; Li, Q.; Chu, C. H. The Antibacterial Mechanism of Silver Nanoparticles and Its Application in Dentistry. *Int. J. Nanomedicine* **2020**, *Volume 15*, 2555–2562. https://doi.org/10.2147/IJN.S246764.
(13) Lu, J.; Cai, Z.; Zou, Y.; Wu, D.; Wang, A.; Chang, J.; Wang, F.; Tian, Z.; Liu, G. Silver Nanoparticle-Based Surface-Enhanced Raman Spectroscopy for the Rapid and Selective Detection of Trace Tropane Alkaloids in Food. *ACS Appl. Nano Mater.* **2019**, *2* (10), 6592–6601. https://doi.org/10.1021/acsanm.9b01493.
(14) Varghese Alex, K.; Tamil Pavai, P.; Rugmini, R.; Shiva Prasad, M.; Kamakshi, K.; Sekhar, K. C. Green Synthesized Ag Nanoparticles for Bio-Sensing and Photocatalytic Applications. *ACS Omega* **2020**, *5* (22), 13123–13129. https://doi.org/10.1021/acsomega.0c01136.
(15) Liu, Y.; Liu, C.-H.; Debnath, T.; Wang, Y.; Pohl, D.; Besteiro, L. V.; Meira, D. M.; Huang, S.; Yang, F.; Rellinghaus, B.; Chaker, M.; Perepichka, D. F.; Ma, D. Silver Nanoparticle Enhanced Metal-Organic Matrix with Interface-Engineering for Efficient Photocatalytic Hydrogen Evolution. *Nat. Commun.* **2023**, *14* (1), 541. https://doi.org/10.1038/s41467-023-35981-8.
(16) Zhang, Q.; Xie, J.; Yang, J.; Lee, J. Y. Monodisperse Icosahedral Ag, Au, and Pd Nanoparticles: Size Control Strategy and Superlattice Formation. *ACS Nano* **2009**, *3* (1), 139–148. https://doi.org/10.1021/nn800531q.
(17) Courty, A. Silver Nanocrystals: Self-Organization and Collective Properties. *J. Phys. Chem. C* **2010**, *114* (9), 3719–3731. https://doi.org/10.1021/jp908966b.
(18) Epple, M.; Rotello, V. M.; Dawson, K. The Why and How of Ultrasmall Nanoparticles. *Acc. Chem. Res.* **2023**, *56* (23), 3369–3378. https://doi.org/10.1021/acs.accounts.3c00459.
(19) Kim, B. H.; Hackett, M. J.; Park, J.; Hyeon, T. Synthesis, Characterization, and Application of Ultrasmall Nanoparticles. *Chem. Mater.* **2014**, *26* (1), 59–71. https://doi.org/10.1021/cm402225z.
(20) Wang, W.; Zhou, S.; Shen, M.; Hood, Z. D.; Xiao, K.; Xia, Y. Facile Synthesis of Silver Icosahedral Nanocrystals with Uniform and Controllable Sizes. *ChemNanoMat* **2018**, *4* (10), 1071–1077. https://doi.org/10.1002/cnma.201800255.
(21) Peng, S.; McMahon, J. M.; Schatz, G. C.; Gray, S. K.; Sun, Y. Reversing the Size-Dependence of Surface Plasmon Resonances. *Proc. Natl. Acad. Sci.* **2010**, *107* (33), 14530–14534. https://doi.org/10.1073/pnas.1007524107.
(22) Lu, X.; Tuan, H.-Y.; Chen, J.; Li, Z.-Y.; Korgel, B. A.; Xia, Y. Mechanistic Studies on the Galvanic Replacement Reaction between Multiply Twinned Particles of Ag and $HAuCl_4$ in an Organic Medium. *J. Am. Chem. Soc.* **2007**, *129* (6), 1733–1742. https://doi.org/10.1021/ja067800f.
(23) Tsuji, M.; Ogino, M.; Matsuo, R.; Kumagae, H.; Hikino, S.; Kim, T.; Yoon, S.-H. Stepwise Growth of Decahedral and Icosahedral Silver Nanocrystals in DMF. *Cryst. Growth Des.* **2010**, *10* (1), 296–301. https://doi.org/10.1021/cg9009042.
(24) Kuai, L.; Geng, B.; Wang, S.; Zhao, Y.; Luo, Y.; Jiang, H. Silver and Gold Icosahedra: One-Pot Water-Based Synthesis and Their Superior Performance in the Electrocatalysis for Oxygen Reduction Reactions in Alkaline Media. *Chem. – Eur. J.* **2011**, *17* (12), 3482–3489. https://doi.org/10.1002/chem.201002949.
(25) Shang, L.; Dörlich, R. M.; Trouillet, V.; Bruns, M.; Ulrich Nienhaus, G. Ultrasmall Fluorescent Silver Nanoclusters: Protein Adsorption and Its Effects on Cellular Responses. *Nano Res.* **2012**, *5* (8), 531–542. https://doi.org/10.1007/s12274-012-0238-x.
(26) Wuithschick, M.; Paul, B.; Bienert, R.; Sarfraz, A.; Vainio, U.; Sztucki, M.; Kraehnert, R.; Strasser, P.; Rademann, K.; Emmerling, F.; Polte, J. Size-Controlled Synthesis of Colloidal Silver Nanoparticles Based on Mechanistic Understanding. *Chem. Mater.* **2013**, *25* (23), 4679–4689. https://doi.org/10.1021/cm401851g.
(27) Wetzel, O.; Hosseini, S.; Loza, K.; Heggen, M.; Prymak, O.; Bayer, P.; Beuck, C.; Schaller, T.; Niemeyer, F.; Weidenthaler, C.; Epple, M. Metal–Ligand Interface and Internal Structure of Ultrasmall Silver Nanoparticles (2 Nm). *J. Phys. Chem. B* **2021**, *125* (21), 5645–5659. https://doi.org/10.1021/acs.jpcb.1c02512.

(28) Manno, R.; Sebastian, V.; Irusta, S.; Mallada, R.; Santamaria, J. Ultra-Small Silver Nanoparticles Immobilized in Mesoporous SBA-15. Microwave-Assisted Synthesis and Catalytic Activity in the 4-Nitrophenol Reduction. *Catal. Today* **2021**, *362*, 81–89. https://doi.org/10.1016/j.cattod.2020.04.018.
(29) Xie, Z.; Tzeng, W.; Huang, C. One-Pot Synthesis of Icosahedral Silver Nanoparticles by Using a Photoassisted Tartrate Reduction Method under UV Light with a Wavelength of 310 Nm. *ChemPhysChem* **2016**, *17* (16), 2551–2557. https://doi.org/10.1002/cphc.201600257.
(30) Keunen, R.; Cathcart, N.; Kitaev, V. Plasmon Mediated Shape and Size Selective Synthesis of Icosahedral Silver Nanoparticles via Oxidative Etching and Their 1-D Transformation to Pentagonal Pins. *Nanoscale* **2014**, *6* (14), 8045–8051. https://doi.org/10.1039/C4NR01477D.
(31) Langille, M. R.; Zhang, J.; Personick, M. L.; Li, S.; Mirkin, C. A. Stepwise Evolution of Spherical Seeds into 20-Fold Twinned Icosahedra. *Science* **2012**, *337* (6097), 954–957. https://doi.org/10.1126/science.1225653.
(32) Zhang, Q.; Xie, J.; Yang, J.; Lee, J. Y. Monodisperse Icosahedral Ag, Au, and Pd Nanoparticles: Size Control Strategy and Superlattice Formation. *ACS Nano* **2009**, *3* (1), 139–148. https://doi.org/10.1021/nn800531q.
(33) Munir, I.; Yesiloz, G. Novel Size-Tunable and Straightforward Ultra-Small Nanoparticle Synthesis in a Varying Concentration Range of Glycerol as a Green Reducing Solvent. *ACS Omega* **2023**, *8* (31), 28456–28466. https://doi.org/10.1021/acsomega.3c02697.
(34) Madkour, M.; Bumajdad, A.; Al-Sagheer, F. To What Extent Do Polymeric Stabilizers Affect Nanoparticles Characteristics? *Adv. Colloid Interface Sci.* **2019**, *270*, 38–53. https://doi.org/10.1016/j.cis.2019.05.004.
(35) Saldías∗, C.; Bonardd, S.; Quezada, C.; Radi´c, D.; Leiva, A. The Role of Polymers in the Synthesis of Noble Metal Nanoparticles: A Review. *J. Nanosci. Nanotechnol.* **2017**, *17* (1), 87–114. https://doi.org/10.1166/jnn.2017.13016.
(36) Amiens, C.; Chaudret, B.; Ciuculescu-Pradines, D.; Collière, V.; Fajerwerg, K.; Fau, P.; Kahn, M.; Maisonnat, A.; Soulantica, K.; Philippot, K. Organometallic Approach for the Synthesis of Nanostructures. *New J. Chem.* **2013**, *37* (11), 3374. https://doi.org/10.1039/c3nj00650f.
(37) Cormary, B.; Dumestre, F.; Liakakos, N.; Soulantica, K.; Chaudret, B. Organometallic Precursors of Nano-Objects, a Critical View. *Dalton Trans.* **2013**, *42* (35), 12546. https://doi.org/10.1039/c3dt50870f.
(38) Nath, S.; Jana, S.; Pradhan, M.; Pal, T. Ligand-Stabilized Metal Nanoparticles in Organic Solvent. *J. Colloid Interface Sci.* **2010**, *341* (2), 333–352. https://doi.org/10.1016/j.jcis.2009.09.049.
(39) Mozaffari, S.; Li, W.; Thompson, C.; Ivanov, S.; Seifert, S.; Lee, B.; Kovarik, L.; Karim, A. M. Colloidal Nanoparticle Size Control: Experimental and Kinetic Modeling Investigation of the Ligand–Metal Binding Role in Controlling the Nucleation and Growth Kinetics. *Nanoscale* **2017**, *9* (36), 13772–13785. https://doi.org/10.1039/C7NR04101B.
(40) Ramamoorthy, R. K.; Yildirim, E.; Barba, E.; Roblin, P.; Vargas, J. A.; Lacroix, L.-M.; Rodriguez-Ruiz, I.; Decorse, P.; Petkov, V.; Teychené, S.; Viau, G. The Role of Pre-Nucleation Clusters in the Crystallization of Gold Nanoparticles. *Nanoscale* **2020**, *12* (30), 16173–16188. https://doi.org/10.1039/D0NR03486J.
(41) Yildirim, E.; Ramamoorthy, R. K.; Parmar, R.; Roblin, P.; Vargas, J. A.; Petkov, V.; Diaz, A.; Checchia, S.; Ruiz, I. R.; Teychené, S.; Lacroix, L.-M.; Viau, G. Simple Synthesis of Monodisperse Ultrasmall Au Icosahedral Nanoparticles. *J. Phys. Chem. C* **2023**, *127* (6), 3047–3058. https://doi.org/10.1021/acs.jpcc.2c07323.
(42) Kotlarchyk, M.; Stephens, R. B.; Huang, J. S. Study of Schultz Distribution to Model Polydispersity of Microemulsion Droplets. *J. Phys. Chem.* **1988**, *92* (6), 1533–1538. https://doi.org/10.1021/j100317a032.
(43) Juhás, P.; Davis, T.; Farrow, C. L.; Billinge, S. J. L. *PDFgetX3* : A Rapid and Highly Automatable Program for Processing Powder Diffraction Data into Total Scattering Pair Distribution Functions. *J. Appl. Crystallogr.* **2013**, *46* (2), 560–566. https://doi.org/10.1107/S0021889813005190.

(44) Hjorth Larsen, A.; Jørgen Mortensen, J.; Blomqvist, J.; Castelli, I. E.; Christensen, R.; Dułak, M.; Friis, J.; Groves, M. N.; Hammer, B.; Hargus, C.; Hermes, E. D.; Jennings, P. C.; Bjerre Jensen, P.; Kermode, J.; Kitchin, J. R.; Leonhard Kolsbjerg, E.; Kubal, J.; Kaasbjerg, K.; Lysgaard, S.; Bergmann Maronsson, J.; Maxson, T.; Olsen, T.; Pastewka, L.; Peterson, A.; Rostgaard, C.; Schiøtz, J.; Schütt, O.; Strange, M.; Thygesen, K. S.; Vegge, T.; Vilhelmsen, L.; Walter, M.; Zeng, Z.; Jacobsen, K. W. The Atomic Simulation Environment—a Python Library for Working with Atoms. *J. Phys. Condens. Matter* **2017**, *29* (27), 273002. https://doi.org/10.1088/1361-648X/aa680e.

(45) Juhás, P.; Farrow, C. L.; Yang, X.; Knox, K. R.; Billinge, S. J. L. Complex Modeling: A Strategy and Software Program for Combining Multiple Information Sources to Solve Ill Posed Structure and Nanostructure Inverse Problems. *Acta Crystallogr. Sect. Found. Adv.* **2015**, *71* (6), 562–568. https://doi.org/10.1107/S2053273315014473.

(46) Ramamoorthy, R. K.; Yildirim, E.; Rodriguez-Ruiz, I.; Roblin, P.; Lacroix, L.-M.; Diaz, A.; Parmar, R.; Teychené, S.; Viau, G. Sub-Millisecond Microfluidic Mixers Coupled to Time-Resolved *in Situ* Photonics to Study Ultra-Fast Reaction Kinetics: The Case of Ultra-Small Gold Nanoparticle Synthesis. *Lab. Chip* **2024**, *24* (2), 327–338. https://doi.org/10.1039/D3LC00778B.

(47) Montano, P. A.; Zhao, J.; Ramanathan, M.; Shenoy, G. K.; Schulze, W. EXAFS Study of Ag, Fe, and Ge Microclusters. *Phys. B Condens. Matter* **1989**, *158* (1–3), 242–244. https://doi.org/10.1016/0921-4526(89)90272-X.

(48) Desireddy, A.; Conn, B. E.; Guo, J.; Yoon, B.; Barnett, R. N.; Monahan, B. M.; Kirschbaum, K.; Griffith, W. P.; Whetten, R. L.; Landman, U.; Bigioni, T. P. Ultrastable Silver Nanoparticles. *Nature* **2013**, *501* (7467), 399–402. https://doi.org/10.1038/nature12523.

(49) Sharma, J.; Chaki, N. K.; Mandale, A. B.; Pasricha, R.; Vijayamohanan, K. Controlled Interlinking of Au and Ag Nanoclusters Using 4-Aminothiophenol as Molecular Interconnects. *J. Colloid Interface Sci.* **2004**, *272* (1), 145–152. https://doi.org/10.1016/j.jcis.2003.09.016.

(50) Thanh, N. T. K.; Maclean, N.; Mahiddine, S. Mechanisms of Nucleation and Growth of Nanoparticles in Solution. *Chem. Rev.* **2014**, *114* (15), 7610–7630. https://doi.org/10.1021/cr400544s.

(51) Karthika, S.; Radhakrishnan, T. K.; Kalaichelvi, P. A Review of Classical and Nonclassical Nucleation Theories. *Cryst. Growth Des.* **2016**, *16* (11), 6663–6681. https://doi.org/10.1021/acs.cgd.6b00794.

(52) Sugimoto, T. Underlying Mechanisms in Size Control of Uniform Nanoparticles. *J. Colloid Interface Sci.* **2007**, *309* (1), 106–118. https://doi.org/10.1016/j.jcis.2007.01.036.

(53) LaMer, V. K.; Dinegar, R. H. Theory, Production and Mechanism of Formation of Monodispersed Hydrosols. *J. Am. Chem. Soc.* **1950**, *72* (11), 4847–4854. https://doi.org/10.1021/ja01167a001.

(54) Sear, R. P. Nucleation: Theory and Applications to Protein Solutions and Colloidal Suspensions. *J. Phys. Condens. Matter* **2007**, *19* (3), 033101. https://doi.org/10.1088/0953-8984/19/3/033101.

(55) Van Embden, J.; Sader, J. E.; Davidson, M.; Mulvaney, P. Evolution of Colloidal Nanocrystals: Theory and Modeling of Their Nucleation and Growth. *J. Phys. Chem. C* **2009**, *113* (37), 16342–16355. https://doi.org/10.1021/jp9027673.

(56) Chen, X.; Schröder, J.; Hauschild, S.; Rosenfeldt, S.; Dulle, M.; Förster, S. Simultaneous SAXS/WAXS/UV–Vis Study of the Nucleation and Growth of Nanoparticles: A Test of Classical Nucleation Theory. *Langmuir* **2015**, *31* (42), 11678–11691. https://doi.org/10.1021/acs.langmuir.5b02759.

(57) Peng, S.; Lee, Y.; Wang, C.; Yin, H.; Dai, S.; Sun, S. A Facile Synthesis of Monodisperse Au Nanoparticles and Their Catalysis of CO Oxidation. *Nano Res.* **2008**, *1* (3), 229–234. https://doi.org/10.1007/s12274-008-8026-3.

(58) Avaro, J.; Moon, E. M.; Schulz, K. G.; Rose, A. L. Calcium Carbonate Prenucleation Cluster Pathway Observed via In Situ Small-Angle X-Ray Scattering. *J. Phys. Chem. Lett.* **2023**, *14* (19), 4517–4523. https://doi.org/10.1021/acs.jpclett.2c03192.

(59) Wang, J.; Mbah, C. F.; Przybilla, T.; Apeleo Zubiri, B.; Spiecker, E.; Engel, M.; Vogel, N. Magic Number Colloidal Clusters as Minimum Free Energy Structures. *Nat. Commun.* **2018**, *9* (1), 5259. https://doi.org/10.1038/s41467-018-07600-4.

Graphical Abstract

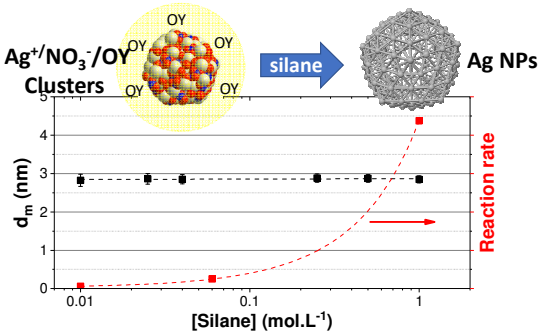

Nucleation in Confinement: A Pathway to Size-Controlled Ultra-Small Icosahedral Silver Nanoparticles

Rohan Parmar,[1,2] Raj Kumar Ramamoorthy,[2] Pierre Roblin[1], Nicolas Ratel-Ramond[2], Lise-Marie Lacroix,[2] Isaac Rodriguez-Ruiz,[1] Sébastien Teychené,[1*] Guillaume Viau[2*]

[1] *Université de Toulouse, Laboratoire de Génie Chimique, CNRS, INP, 4 allée Emile Monso F-31432 Toulouse cedex 4 France*

[2] *Université de Toulouse, Laboratoire de Physique et Chimie des Nano-Objets, INSA Toulouse, CNRS, 135 avenue de Rangueil F-31077 Toulouse cedex 4, France*

Supporting Information

I. SAXS Analysis

a. Ag NPs

All scattering patterns of the Ag NP suspensions were analysed using the software SasView 5.0.5,[1] where experimental data was fit with a form factor of a sphere[2].

$$I(q) = \frac{scale}{V}\left[3V(\Delta\rho)\frac{\sin(qr) - qr\cos(qr))}{(qr)^3}\right]^2 + background \qquad (1)$$

where *scale* is the volume fraction (assuming data is in absolute scale), *V* and *r* are the volumes and radii of the nanospheres, and $\Delta\rho$ is the difference between the scattering length densities of Ag and hexane which were kept constant at 77.9 x 10^{-6} and 6.51 x 10^{-6} Å^{-2}, respectively. Using the volume fractions obtained from the fits, it is possible to calculate the final concentrations of Ag^0:

$$[Ag_{final}] = \frac{(Scale)(M_{Ag})}{\rho_{Ag}} \qquad (2)$$

where M_{Ag} and ρ_{Ag} are the molecular weight and density, respectively, of silver. In this case, the reaction yield then simply becomes the ratio of the final and nominal concentrations of Ag.

Scale, background, and radius were parameters that were left free in the model, while particle size distribution was determined using a Schulz function[3]:

$$f(r) = \frac{1}{Norm}\left(\frac{z+1}{\bar{r}}\right)^{z+1} r^z \exp\left[-\left(\frac{z+1}{\bar{r}}\right)\mathrm{r}\right]/\Gamma(\mathrm{z}+1) \qquad (3)$$

where $\bar{r}$ is the mean sphere radius, *Norm* is a normalization factor, Γ is the gamma function, and *z* refers to the width of the distribution, such that a polydispersity ratio, PD, is defined:

$$PD = \frac{\sigma}{\bar{r}} \quad (4)$$

$$\chi^2 = \sum \frac{(x_i - x_t)^2}{(weight_i^2)} \quad (5)$$

where σ is the standard deviation from the mean particle size. The quality of the fit was determined by the chi squared (χ^2) value:

where x_i and x_t are the experimental and theoretical data points, and $weight_i$ is a factor that determines the magnitude of impact each data point has in the fit. In this case the weight was kept as the modulus of the intensity (|I|), and the goodness of the fit was deemed optimal as χ^2 converged to 0.

An example of a fit is given Fig. S1.

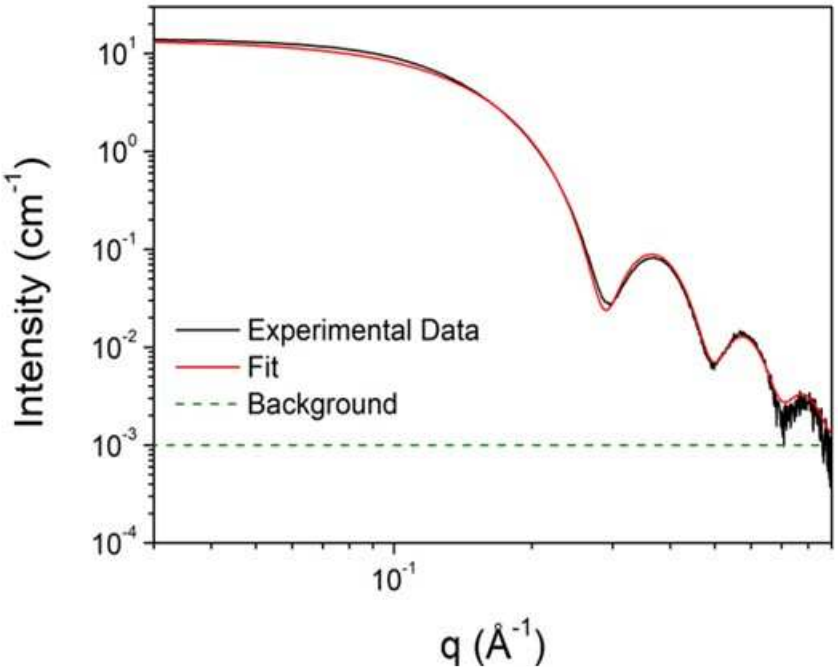

Figure S1. Representative SAXS pattern of Ag NPs prepared by the reduction of $AgNO_3$ by TES at 40°C ([Ag] = 0.16 mol.L^{-1}, [OY]/[Ag] = 2.5, [TES] = 1 mol.L^{-1}): experimental data (black) fit by a single population of nanospheres (red): diameter = 3.09 nm, σ/d_m = 0.06, and background (dashed green). The χ^2 value was 0.0073 representing an excellent goodness of fit.

b. Ag PNCs

A Guinier-Porod[4] model was used to fit the scattering profiles of the Ag PNCs on SasView.

$$I(q) = \frac{G}{Q^s} exp\left[\frac{-Q^2 R_g^2}{3-s}\right] \quad Q \leq Q_1 \qquad (6)$$
$$I(q) = D/Q^m \qquad Q \geq Q_1$$

where G and D are the Guinier and Porod scale factors, respectively, Q is the scattering variable where Q_1 is the point that the derivatives of the Guinier and Porod terms are equal and continuous, m is the porod exponent, and R_g and s are the radius of gyration and dimensionality, respectively, of the scattering objects.

The radius of gyration of a spherical object gives a value of the radius such that $R = \sqrt{\frac{5}{3}} R_g$

An example of a fit is given Fig. S2.

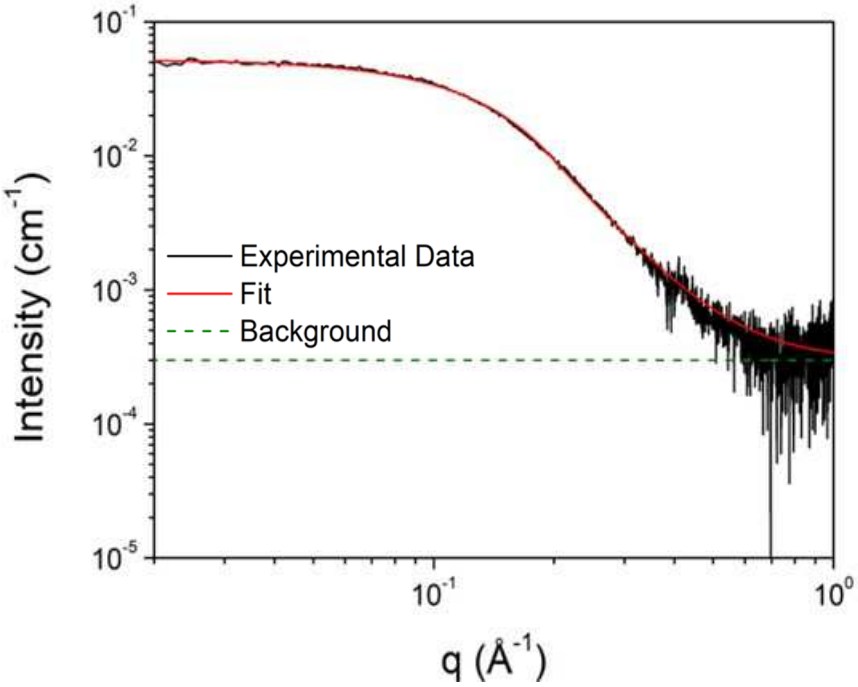

Figure S2. Representative SAXS pattern of Ag PNCs obtained by dissolution of $AgNO_3$ in a solution of OY in hexane, [Ag] = 0.04 mol.L^{-1}, [OY]/[Ag] = 2.5, T = 40 °C. Experimental data (black) fit by a Guinier-Porod profile (red): *R_g = 11.9 nm ; porod exponent = 3.67.*

References

(1) SasView. *SasView*. https://sasview.github.io/ (accessed 2024-08-23).
(2) Rice, S. A. Small Angle Scattering of X-rays. A. Guinier and G. Fournet. Translated by C. B. Wilson and with a Bibliographical Appendix by K. L. Yudowitch. Wiley, New York,

1955. 268 Pp. $7.50. *J. Polym. Sci.* **1956**, *19* (93), 594–594. https://doi.org/10.1002/pol.1956.120199326.
(3) Kotlarchyk, M.; Stephens, R. B.; Huang, J. S. Study of Schultz Distribution to Model Polydispersity of Microemulsion Droplets. *J. Phys. Chem.* **1988**, *92* (6), 1533–1538. https://doi.org/10.1021/j100317a032.
(4) Hammouda, B. A New Guinier–Porod Model. *J Appl Crystallogr* **2010**, *43* (4), 716–719. https://doi.org/10.1107/S0021889810015773.

II. Microfluidic Setup

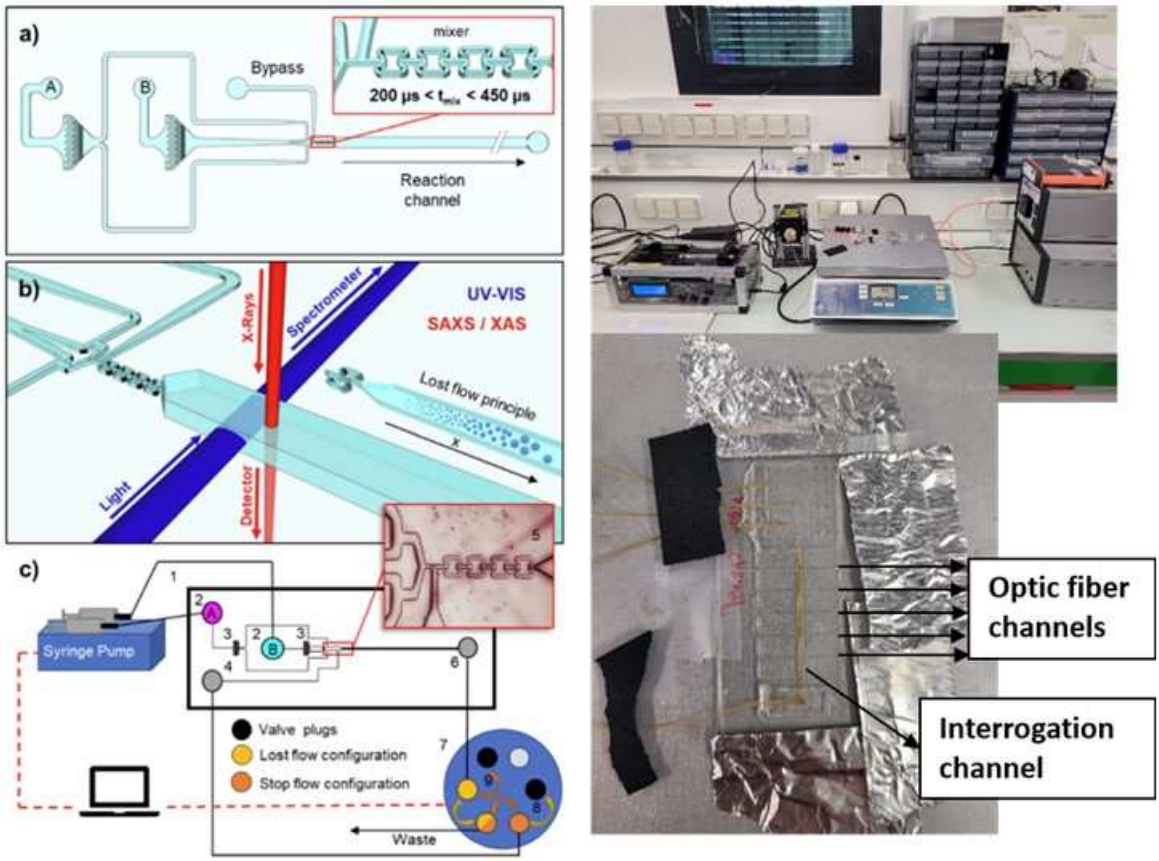

Figure S3. Schematic of the microfluidic setup and configuration, On the left: (a) Two inlets (A, B) for the injection of the reagents, a bypass channel, four butterfly mixers of 20 µm × 50 µm cross-section (as Inset), a principal interrogation channel to track the reaction, and an outlet; (b) a configuration highlighting the coupling of techniques such as UV-Vis and SAXS; (c) An experimental setup with previously mentioned OSTEMER microreactor, a syringe pump system for the reagent injection at set flow rates, and a valve configuration to cycle between continuous (lost) flow and stop flow measurements. On the right: experimental setup showing the syringe pump system, a microfluidic reactor on a hotplate set at 40°C (with a vertical zoom of the reactor showing the different optical fiber channels and the yellow Ag NP solution being tracked in the principal interrogation channel), and the spectrometer/light source.

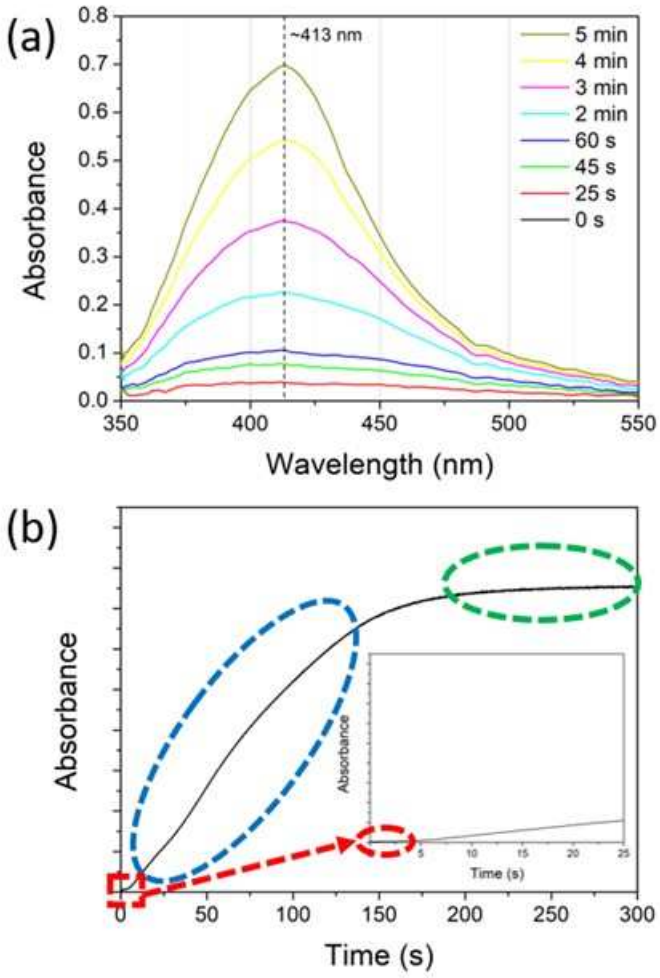

Figure S4. (a) UV-Vis measurements showing the emergence of a plasmonic peak as a function of time of the Ag NPs of size 3 nm centered around λ = 413 nm. Flow rates were kept constant at 4μL/s, ensuring a high mixing efficiency based on tests conducted with fluorescent dyes. (b) Absorbance as a function of time at the chosen wavelength plasmonic wavelength of λ = 413 nm. The corresponding curve has three distinct sections: a first section where the absorbance remains at zero (induction period), a second section where a rapid increase in the absorbance is observed (nucleation period), and a third period where the absorbance reached a plateau and remained constant (growth period).

III. Nanoparticle structural characterization

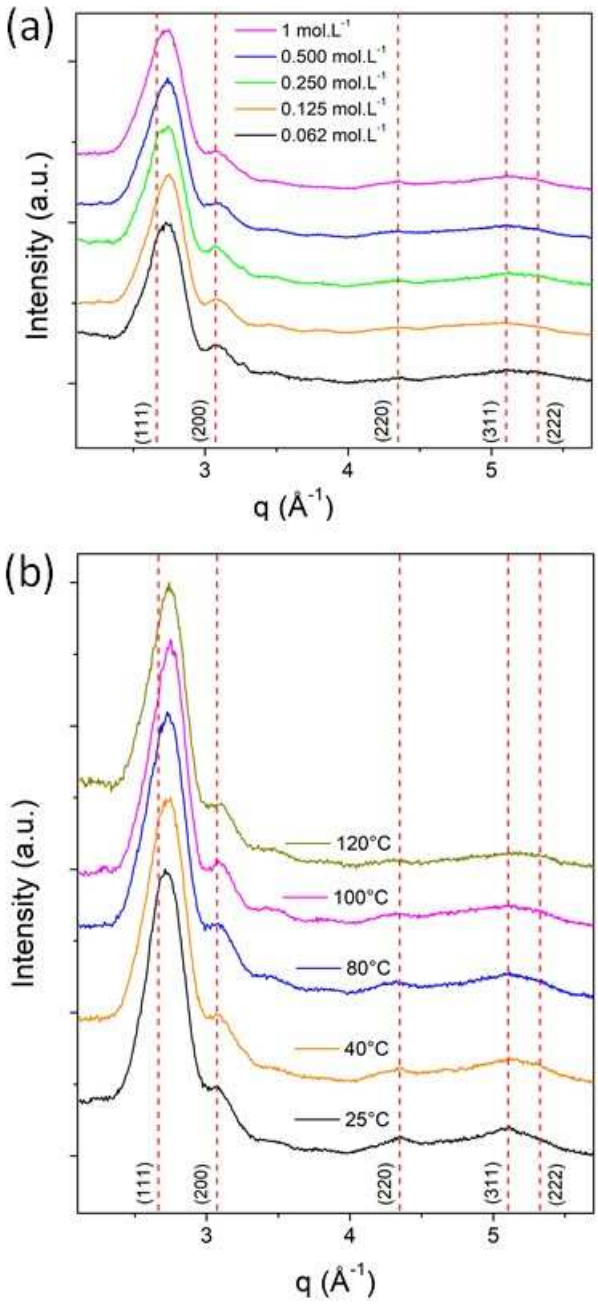

Figure S5. XRD patterns of Ag NPs (a) prepared with different concentrations of [TES] ([Ag] = 0.02 mol.L^{-1}, [OY]/[Ag] = 2.5 were kept constant); (b) at different temperature between 25 and 120 °C. Solutions were prepared in hexane until 60°C and in decane for all other temperatures. TES was the reducing agent until 100°C and TIPS for the other temperatures ([Ag] = 0.02 mol.L^{-1}, [OY]/[Ag] = 2.5, [TES/TIPS] = 1 mol.L^{-1} were all kept constant). ([TES] = 1 mol.L^{-1}, [Ag] = [OY]/[Ag] = 2.5 were kept constant).

($q = \frac{4\pi sin\theta}{\lambda}$, $\lambda_{K\alpha}$(Co) = 1.790Å)

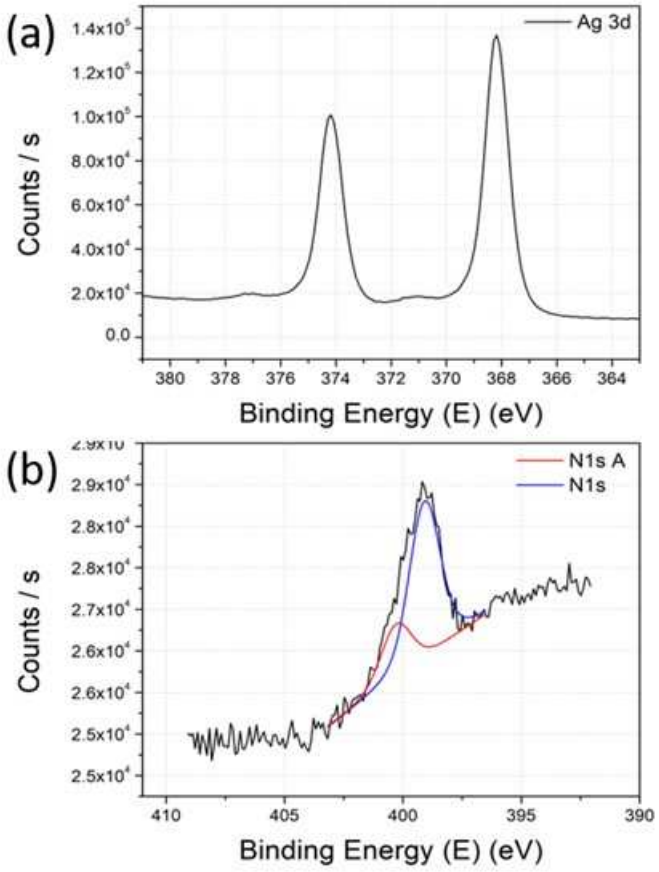

Figure S6. XPS spectra of Ag NPs nanoparticles prepared with [Ag] = 20 mM and [OY]/[Ag] = 2.5: (a) Ag 3d peaks; (b) N 1s peak showing a main contribution (74%) at the binding energy of free OY (399 eV) and a minor contribution (26%) at the binding energy of coordinated OY (400.5 eV).

IV. SAXS of Ag nanoparticles using different experimental conditions

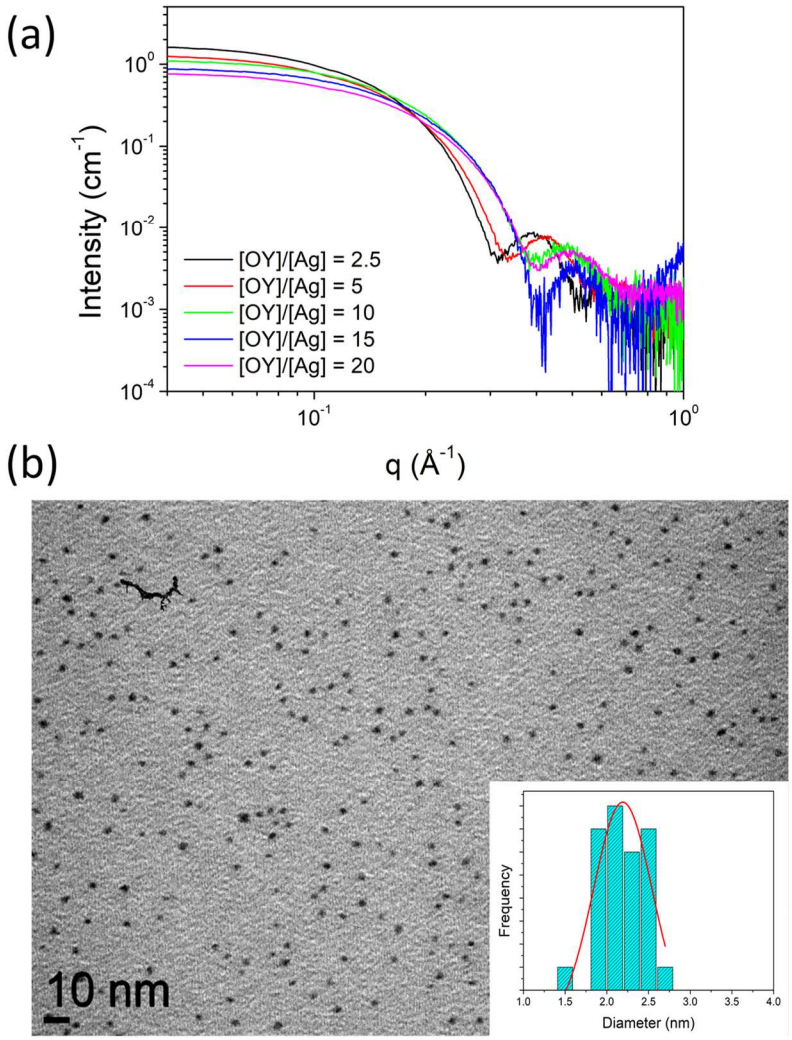

Figure S7. (a) SAXS profiles of Ag NP suspensions prepared by the reduction of $AgNO_3$ with TES dissolved in a solution of OY in hexane for [OY]/[Ag] varying in the range 2.5 to 20 ([Ag], [TES] and T were fixed at 0.02 mol.L^{-1}, 1 mol.L^{-1} and 40 °C, respectively); (b) TEM image and size distribution (inset) of Ag NPs prepared at 40 °C with [Ag] = 0.02 mol. L^{-1}, [TES] = 1 mol. L^{-1} and [OY]/[Ag] = 20.

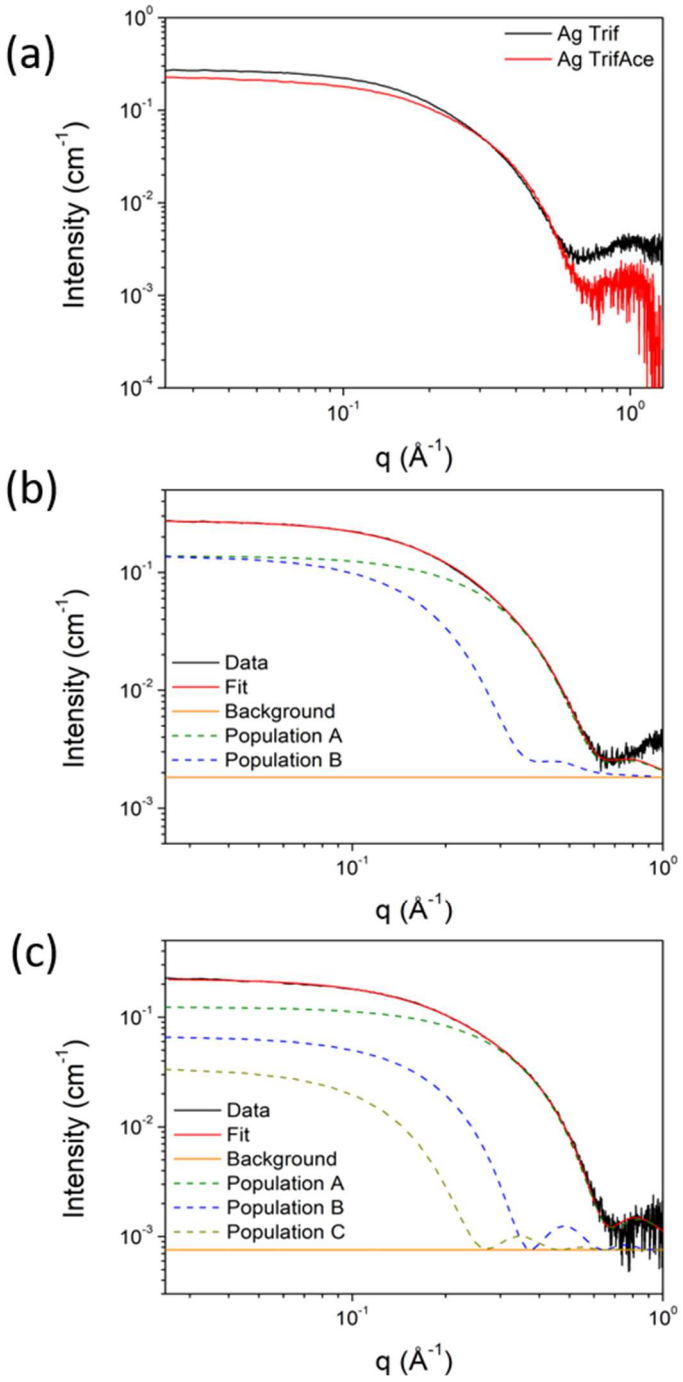

Figure S8. (a) SAXS scattering profile of Ag NPs prepared at 40°C using Ag Trif and Ag TrifAce as the precursors with [Ag] = 0.02 mol.L^{-1}, [TES] = 1 mol.L^{-1}, and [OY]/[Ag] = 2.5; (b) SAXS curve for Ag NPs prepared using silver trifluoromethanesulfonate with fitting using 2 populations of spheres (Pop A: d = 1.35 +/- 0.1 nm – 84% proportion, Pop B: d = 2.32 +/- 0.16 nm – 16% proportion); (c) SAXS curve for Ag NPs prepared using silver trifluoroacetate with fitting using 3 populations of spheres (Pop A: d = 1.3 +/- 0.08 nm – 81% proportion, Pop B: d = 2.4 +/- 0.07 nm – 10% proportion, Pop C: d = 3.3 +/- 0.1 nm – 9% proportion); black = experimental data, red = fit, dashed green, blue, and gold lines = proportions of population A, B, and C, orange = background